Summer 8-4-2021

Scale-Dependence of Hematite Nanoparticle Sulfidation

Uma Lad
Southern Methodist University, ulad@smu.edu

SCALE-DEPENDENCE OF HEMATITE NANOPARTICLE SULFIDATION

Approved by:

_____

Andrew Quicksall, Ph.D,
Associate Professor of Civil and
Environmental Engineering

_____

Robert Gregory, Ph.D,
Professor of Earth Sciences

_____

Crayton Yapp, Ph.D,
Professor of Earth Sciences

SCALE-DEPENDENCE OF HEMATITE NANOPARTICLE SULFIDATION

A Thesis Presented to the Graduate Faculty of the

Dedman College

Southern Methodist University

in

Partial Fulfillment of the Requirements

for the degree of

Master of Science

by

Uma Bharat Lad

B.S. Environmental Science, Southern Methodist University

August 4, 2021

ACKNOWLEDGMENTS

I would like to thank my advisor, Dr. Andrew Quicksall, for his advice, knowledge, encouragement, and patience over the many obstacles I faced in my work and for helping me develop my academic and professional goals. Thank you to my committee members, Dr. Bob Gregory and Dr. Crayton Yapp, for their knowledge and for being instructors who piqued my interest in geology through their courses.

My work could not have been possible without the efforts and support of my lab group, Hope, Sally, Abdullah, Lael, Kenney, Riyadh, Lizzie, Mahdi, and Faris. Thank you for spending countless hours teaching me new techniques and for being available to help me troubleshoot any issues I had in my work. A special thanks to Sally and Hope, who provided some much-needed laughter through their stories and general silliness these past months.

I would like to thank my parents Bharat and Padma, my brother Vivek, and my uncle and aunt, Jatin and Deepti, for their unconditional love, support, and guidance. To my cousins Pari and Prem, thank you for being my cheerleaders. I would like to thank Jasmine for being an amazing friend these past years. Finally, I would like to thank the OEP team, Priscilla, Mary, Bart, Heather, Emma, and many others for making me feel included and appreciated in all of my work.

Lad, Uma B.S., Environmental Science, Southern Methodist University

Scale Dependence of Hematite Nanoparticle Sulfidation

Advisor: Professor Andrew Quicksall

Master of Science conferred August 4, 2021

Thesis completed July 16, 2021

Iron (oxyhydr)oxides are widespread in the environment and have a disproportionate effect on the fate of metal(loid)s in groundwater. Numerous studies demonstrate the effect of iron-sulfur dynamics on contaminant sequestration, and particle size further impacts the reactivity of iron (oxyhydr)oxides, including their capacity for sorption and precipitation. This study examines the role of particle size on the sulfidation of iron (oxyhydr)oxides. Synthetic hematite nanoparticles with approximate diameters of 7.1 nm and 104 nm were coated onto quartz sand and reacted with bisulfide by advective flow.

Characterization of these nanoparticles revealed hydroxyls present at the hematite surface, with large particles having a higher hydroxide content per unit of surface area. Analysis of effluent from advective flow experiments show that the hematite nanoparticles undergo reductive dissolution of iron followed by precipitation of FeS. Iron concentrations increased with increasing bisulfide concentration, and ferrous iron in the effluent was higher for small particles than large particles when eluted with 10 mM bisulfide and lower with 0.1 and 1 mM bisulfide. Mineral transformations indicative of FeS precipitation occurred at 1 mM for small particles and at 10 mM for both particle sizes.

The log k_{Fe} calculated through kinetic model were -6.2 for large particles and -7.9 for small particles and indicates that reductive dissolution is faster for large particles. The reaction rate for surface area loss, R_A, over time revealed that precipitation and associated surface passivation controlled initial surface area, influent bisulfide concentration, and initial reaction rate. Initial reaction rates for area and reductive dissolution of iron appear to be impacted by surface hydroxylation. Small particles show that reaction kinetics are not simplistic, and an optimization issue is present in surface mediated reactions where particle size is a factor.

The fundamental experimentation and subsequent model developed in this study could be important to better quantifying the role of iron (oxyhydr)oxide nanoparticles, whether engineered or naturally occurring, on the sequestration of metal(loids) posing a risk to public health.

TABLE OF CONTENTS

LIST OF FIGURES

LIST OF TABLES

CHAPTER 1

INTRODUCTION

Iron (oxyhydr)oxides often control the availability of metals and metalloids in aqueous environments. As an example, the reductive dissolution of iron minerals frequently mobilizes trace metals such as lead, arsenic, and nickel, which are hazardous to populations that rely on groundwater as a drinking water source (Cooper et al., 2006; Smedley & Kinniburgh, 2002). Mineral composition and microbial activity affect iron (oxyhydr)oxide reactivity in terms of reduction rates and mechanisms for trace metal sequestration following reduction (Burton et al., 2011; Cooper et al., 2005; Poulton et al., 2004; Skinner, 2005). Ferrihydrite, goethite, and hematite are common iron (oxyhydr)oxides found in the environment, and pH, redox conditions, temperature, and competitive solution species are a few variables that influence their capacity to retain metals.

Iron (oxyhydr)oxides are especially important to the fate of arsenic in groundwater, a major source of drinking water worldwide, as exemplified in the now well documented case of South Asia (Benner et al., 2008; Quicksall et al., 2008; Smedley & Kinniburgh, 2002). Arsenic enrichment of groundwater typically occurs naturally, but some studies suggest that anthropogenic activities such as pesticide use and industrial activity are also contributors to As contamination

(Polizzotto et al., 2008; Smedley & Kinniburgh, 2002). Sediment deposition rates and burial of organic matter generate conditions for iron reduction and arsenic mobilization in near surface sediments (Papacostas et al., 2008; Polizzotto et al., 2008; Quicksall et al., 2008). Depending on porewater pH, arsenate (As(V)) and arsenite (As(III)) are typically the arsenic species present in these systems, and iron (oxyhydr)oxides are able to retain both species (Saalfield & Bostick, 2009; Smedley & Kinniburgh, 2002). At circumneutral pH, arsenate preferentially sorbs onto iron minerals, and reduction of As(V) to As(III) is concurrent with the reductive dissolution of iron (oxyhydr)oxides (Saalfield & Bostick, 2009; Smedley & Kinniburgh, 2002). Sulfide influences iron-arsenic interactions by initiating iron reduction and forming iron sulfides (Hansel et al., 2015; Hellige et al., 2012; Kocar et al., 2010). Arsenic removal can occur in the presence of sulfide by sorption onto iron sulfides or by the precipitation of arsenic sulfides or iron arsenic sulfides (Burton et al., 2014; O'Day et al., 2004; Saalfield & Bostick, 2009).

Studies on arsenic sequestration have demonstrated that sulfur redox cycling impacts the fate of iron in anoxic environments. Under reducing conditions, bacterial sulfate reduction produces sulfide and often kinetically precedes the reductive dissolution of iron (oxyhydr)oxides (Hansel et al., 2015; Neal et al., 2001). Iron and sulfur reduction rates and associated dissolved sulfide concentrations can affect the sorption of metals and the precipitation of metal sulfides (Hansel et al., 2015; Morse & Arakaki, 1993; O'Day et al., 2004). During the sulfidation of iron (oxyhydr)oxides, sulfide oxidizes to elemental sulfur (Hellige et al., 2012). Iron sulfides form by reaction between excess sulfide and ferrous iron, and their composition varies with system S/Fe ratio and the associated extent of sulfidation (Fan et al., 2017; Hellige et al., 2012). In low temperature, aqueous environments, reaction between an iron (oxyhydr)oxide and sulfide is likely to produce poorly crystalline mackinawite (FeS) (Benning et al., 2000; Wolthers et al., 2005). The

transformation of mackinawite to pyrite involves H_2S oxidation in the presence of an oxidized sulfur or iron-sulfur species (Benning et al., 2000; Neal et al., 2001; Rickard, 1997).

S/Fe ratios and reduction potentials are among several variables that affect the removal and retention of metals and metalloids by iron sulfides (Fan et al., 2017; Morse & Arakaki, 1993; Wolthers et al., 2007). For example, S/Fe ratios and metal concentrations control whether cadmium and arsenic sorb onto FeS or replace iron to form metal(loid)-sulfide phases (Fan et al., 2017; Wolthers et al., 2007). These factors could also inhibit the transformation of FeS to mackinawite and pyrite during arsenic sorption onto FeS (Wolthers et al., 2007). A study on the sulfidation of uranium-bearing ferrihydrite attributed uranium release to the formation of uranium-sulfide complexes and mackinawite (Townsend et al., 2019). In addition to their role in systems with contaminated groundwater, iron-sulfur interactions are important in the remediation of acid mine drainage, where oxidation of pyrite produces highly acidic mine waters that can enhance metal dissolution and precipitate iron oxides (Benner, Blowes, et al., 2002; Nordstrom et al., 2000).

The thermodynamic and physiochemical properties of metal oxides vary as a function of particle size; the stability and reactivity of nanoparticles control phase transitions, dissolution processes, and growth mechanisms of a mineral (Bian et al., 2011; French et al., 2009; Navrotsky et al., 2008; Raiswell, 2011). As particle size decreases, mineral stability declines due to increases in positive surface energy and total free energy (Bian et al., 2011; Gilbert et al., 2003; Navrotsky et al., 2008). Below a certain particle size, differences in surface energies allow mineral polymorphs to form preferentially over phases more stable in bulk material (Gilbert et al., 2003; Zhang et al., 2003). Solution temperature and pH during synthesis impact particle size and the formation of mineral phases (Isley & Penn, 2008). Ligand sorption, pH, and ionic strength promote dissolution and aggregation of nanoparticles and influence growth mechanisms like Ostwald

ripening and oriented attachment (Bian et al., 2011; Chun et al., 2010; French et al., 2009; Gilbert et al., 2003; Penn & Banfield, 1998). Particle growth by Ostwald ripening involves diffusion of small particles to larger particles, while particles in oriented attachment aggregate along specific surfaces (Penn, 2004; Penn & Banfield, 1998). These processes can cause size-dependent phase changes. Gilbert et al. (2006) found that aggregation and growth of nanoscale TiO_2 beyond a critical particle size initiated the transition of anatase to rutile (Gilbert et al., 2006). Ligand adsorption influences particle dissolution and aggregation and can induce structural and phase changes without significantly changing particle size (Bian et al., 2011; Keller et al., 2010; Zhang et al., 2003). This process enhances crystallinity of a mineral by neutralizing charges on nanoparticle surfaces (Gilbert et al., 2006). Adsorption of water improved mineral stability and allowed for the formation of more crystalline phases of TiO_2 and ZnS nanoparticles (Gilbert et al., 2003, 2006; Goodell et al., 2008; Zhang et al., 2003). The scale effects discussed above have implications on the reactivity of nanoparticles.

Recent studies have shown that iron (oxyhydr)oxide nanoparticles are prevalent in the environment (Hochella et al., 2008; Plathe et al., 2013) and form by several pathways, including the oxidation of ferrous minerals or Fe(II) in porewaters and freshwaters and by transformation of existing nanoparticles (Raiswell, 2011). Ferrihydrite is among the most reactive iron (oxyhydr)oxides due to its large surface area (Michel, Ehm, Antao, et al., 2007; Raiswell, 2011). The kinetically preferred ferrihydrite eventually transforms to goethite and hematite, the most thermodynamically stable iron (oxyhydr)oxides under ambient conditions (Raiswell, 2011). Increasing Fe(II) concentration reduces the rate of abiotic and biotic ferrihydrite reduction and results in the precipitation of secondary minerals like goethite, magnetite, and lepidocrocite (Benner, Hansel, et al., 2002; Hansel et al., 2003, 2004). Reaction with Fe(II) is one of several

pathways by which ferrihydrite transitions to goethite, and the pH dependence of ferrihydrite solubility affects its rate of transformation (Yee et al., 2006). The ferrihydrite to hematite transition is a slower process that occurs by dehydration and in the absence of Fe(II) (Schwertmann & Murad, 1983; Yee et al., 2006). Mazeina and Navrotsky (2007) found that hematite is metastable relative to goethite at small particle sizes due to a higher surface energy. Variations in temperature and surface area changes the enthalpy of water adsorption and affects the strength of water bonding to hematite (Mazeina & Navrotsky, 2007). In the absence of hydroxyls, hematite nanoparticles decline in stability and undergo a phase transition to maghemite (Chernyshova et al., 2007). Goethite and hematite nanoparticles become unstable as suspension pH approaches the point of zero charge (Xu et al., 2015). Particles have the greatest potential to aggregate by collision at this pH due to weak electrostatic repulsion forces (Xu et al., 2015). Dissolution rates for hematite nanoparticles are higher for smaller particles regardless of pH or dissolution mechanism due to their larger surface areas (Lanzl et al., 2012).

Size-dependent changes in the properties of nanoparticles affect iron (oxyhydr)oxide reactivity and capacity to sequester metals. Goethite can incorporate divalent metals in its crystal structure depending on the similarity of their ionic radii relative to Fe(III) (Cooper et al., 2006; Hansel et al., 2005). Iron (oxyhydr)oxide nanoparticles strongly sorb Cu, As, Zn, and Pb, and adsorption increases with decreasing particle size (Barton et al., 2011; Dickson et al., 2017; Plathe et al., 2013). Other environmental conditions such as pH, temperature, and competitive species influence the sorption capacity of iron (oxyhydroxide) nanoparticles. For example, arsenic desorption caused by microbial sulfate reduction of arsenic-bearing ferrihydrite produces various Fe, As, and S species based on pH, iron and sulfate concentrations, and As loading (Burton et al., 2011; Kocar et al., 2010; Saalfield & Bostick, 2009). Surface area and S/Fe ratios affect reductive

dissolution rates for nanoparticle iron (oxyhydr)oxides and for iron sulfide precipitation caused by sulfidation (Kumar et al., 2018). Similar solubility trends have been observed for the sulfidation of zinc oxide and copper oxide nanoparticles (Ma et al., 2013, 2014).

The studies mentioned previously do not examine the sulfidation of iron (oxyhydr)oxide nanoparticles under continuous flow for minerals aside from ferrihydrite. This study investigates the role of particle size on the reductive dissolution of iron oxide nanoparticles of two different sizes by bisulfide, a product of microbial sulfate reduction and a strong reductant, under dynamic flow conditions. Hematite is the most stable iron (oxyhydr)oxide bulk material under ambient conditions and exhibits large differences in its physiochemical and thermodynamic properties at the nanoscale. Column experiments consist of nanoparticle hematite-coated packed sands exposed to varying concentrations of bisulfide under anoxic, advective flow conditions. Analyses include quantification of dissolved iron and bisulfide concentrations in the column effluent. An integrated kinetic model is developed based on effluent data to determine reaction mechanism and rate constants as a function of particle size. Understanding the role of size on the reactivity and stability of iron (oxyhydr)oxide minerals is important to consider in the fate and transport of metals and metalloids in groundwater where nanoparticles are present.

CHAPTER 2

MATERIALS AND METHODS

2.1 Hematite Nanoparticle Synthesis

Nanoparticle hematite suspensions were synthesized in the laboratory by forced hydrolysis. Large hematite nanoparticles with particle diameters ranging from 30 to 50 nm were prepared using Method 3 in Schwertmann and Cornell (2001). The synthesis involved heating 1L of 0.001 M HCl overnight at 98°C, adding approximately 5.405 g of $FeCl_3 \bullet 6H_2O$ (VWR) to the HCl the following day, and returning the solution to the oven for another 10 days of heating at 98°C (Schwertmann & Cornell, 2001). The small hematite nanoparticles ranging in diameter from 7 to 10 nm were prepared according to a method amended by Madden et al. (2006) from Schwertmann and Cornell (2001). The method consisted of dripping 60 mL of a 1 M $FeCl_3$ (Spectrum Chemical Mfg. Corp.) solution with a peristaltic pump (VWR Variable Flow Mini-Pump) into 750 mL of near boiling 18.2 MΩ distilled, deionized water (DDI) stirred with a magnetic stirrer on a hot plate (Madden et al., 2006). Following the initial steps in each method, both suspensions were left to cool overnight and washed by dialysis. Each suspension was transferred to dialysis tubing (Spectra/Por 7 Dialysis Membrane, Pre-treated RC Tubing, MWCO: 8 kD) and submerged in DDI water. The water bath was changed twice daily until the conductivity of the water stabilized and

nearly equaled the conductivity of DDI water. Suspensions were transferred from dialysis tubing and stored in high-density polyethylene (HDPE) bottles. A portion of each hematite nanoparticle suspension was frozen and freeze-dried for characterization. Dried samples were characterized by Attenuated Total Reflectance-Fourier Transform Infrared Spectroscopy (ATR-FTIR), Brunauer-Emmett-Teller (BET) surface area analysis, Thermogravimetric Analysis (TGA)/Derivative Thermogravimetry (DTG), and Differential Scanning Calorimetry (DSC).

Hematite-coated sands were prepared by mixing each suspension with 1 kg sand (Acros sea sand, washed) and were oven-dried between 50°C and 80°C. Each mixture was passed through the no. 40 (0.420 mm) and no. 200 (0.074 mm) sieves to determine if hematite coating onto the sand was effective. Sand grains were estimated to have sizes within these sieves, while hematite nanoparticles were expected to pass through the smallest sieve and into the catch pan. Coated sand in the catch pan was removed from the bulk sample.

2.2. Experiment Solutions

Each column was eluted with a conditioning solution and a reaction solution. Individual stock solutions of bisulfide and sodium were prepared by dissolving $Na_2S•9H_2O$ (Acros) and $NaClO_4•H_2O$ (EM Science) in DDI water. Conditioning solution was composed of 0.023 mM Rb^+ (Elemental Scientific Rb in 1% HNO_3, 1000 µg/mL) and 10 mM Na^+. Rb^+ was used to examine non-reactive breakthrough from each column, while Na^+ was used to maintain ionic strength in the solution. Reaction solution contained bisulfide and was prepared by diluting a sodium sulfide stock solution to concentrations ranging from 0.01 mM to 10 mM with the same concentrations of Rb and Na used in the conditioning solution. All solutions were prepared in an anaerobic chamber (Coy Laboratory Products, Vinyl Anaerobic Chamber) and adjusted to pH 8 ± 0.1 using 1M HCl and 0.1 NaOH solutions. DDI (18.2 MΩ) water was used in all solutions.

2.3. Advective Flow Experiments

Column studies consisted of flowing bisulfide solution up a borosilicate glass column (Kimble Kontes, 10 cm, I.D. 1 cm) packed with hematite-coated sands. Coated sands were packed with DDI water and eluted with conditioning solution for approximately 1 hour, or an exchange of 10 pore volumes. Reaction solution was transferred from the anaerobic chamber to a bottle connected to the peristaltic pump (Thermo Scientific FH100M Multichannel Pump). Bisulfide oxidation in the bottle was mitigated by flowing a maximum solution volume of 500 mL per run and by using an air lock to constantly purge the head space with a positive pressure of nitrogen. Conditioning and reaction solutions were passed upward into the packed column at a flow rate between 1.05 and 1.15 mL/min and collected at 4 mL intervals using a fraction collector (Spectrum CF-2 Fraction Collector). The tubes were subsampled or fully sacrificed to measure post reaction bisulfide and ferrous iron in solution. Dissolved bisulfide was quantified at 12 to 24 mL intervals, and the remaining samples were prepared elemental analysis for iron and rubidium by ICP-MS. Figure 1 shows the setup of the column experiments, and Table 1 lists the conditions of each column experiment.

Batch experiments were conducted prior to running these columns to determine if sulfidation of hematite nanoparticles would have contrasting effects as a function of particle size and bisulfide concentration. The method and results for this experiment are discussed in Appendix B.

Table 1. Summary of Column Experiments

Column Contents	Bisulfide Concentration (mM)	Volume Eluted (mL)	Total time (hours)	Average Flow Rate (mL/min)	Initial pH	Solution Matrix
Sand (control)	1	500	6.92	1.10	8.22	10 mM Na^+, 0.023 mM Rb^+ (aq)
Small Particles (coated sand)	0.01	500	7.18	1.06	8.14	
	1	500	6.68	1.14	7.85	
	10	351	5.18	1.13	8.18	
Large Particles (coated sand)	0.01	500	6.82	1.10	8.35	
	1	500	7.02	1.08	7.69	
	10	500	6.87	1.12	8.09	

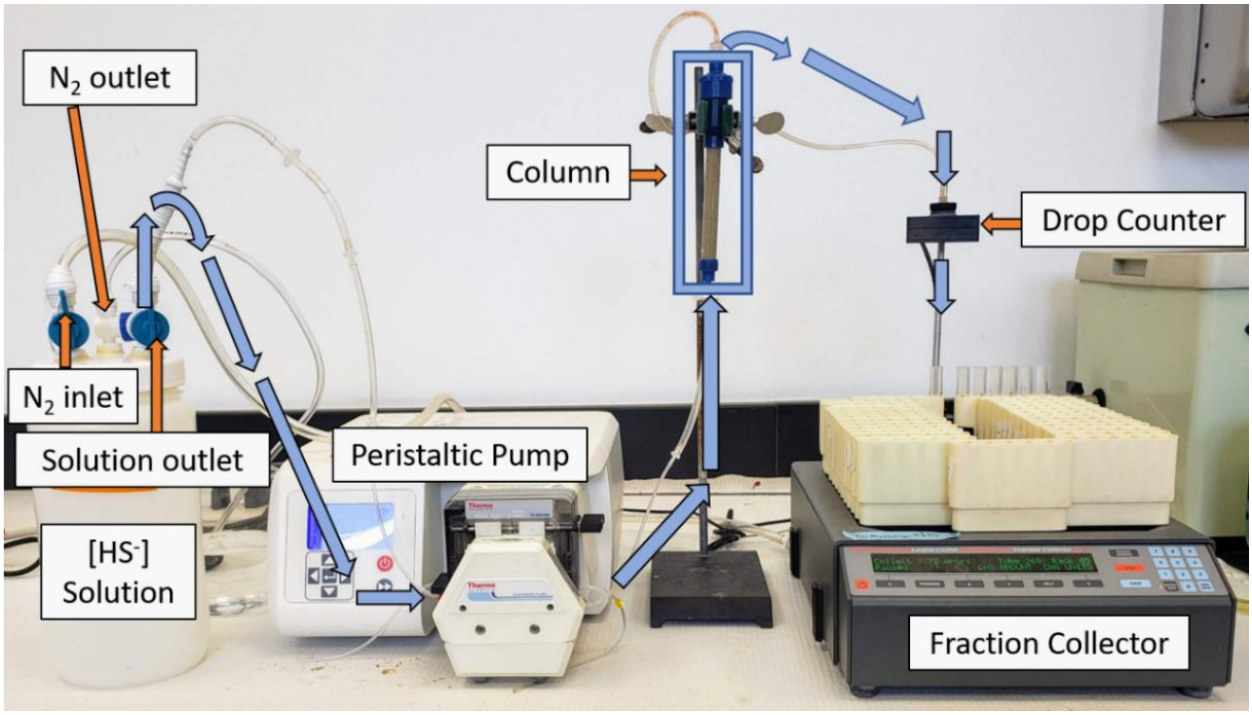

Figure 1. Setup of column experiments. The bisulfide solution bottle contained three ports: solution outlet, N_2 inlet, and N_2 outlet. Nitrogen flowed through the inlet to fill the head space of the bottle and mitigate sulfide oxidation. Gas was continuously pumped out through the nitrogen outlet and into a beaker filled with water. The peristaltic pump transferred bisulfide solution from the bottle and upwards into the column. Column effluent travels from the top of the column, through a drop counter, and into individual tubes in the fraction collector.

2.4. Analytical Methods

2.4.1. Brunauer-Emmett-Teller (BET) Surface Area Analysis

Specific surface area and particle size of the two, freeze-dried hematite suspensions were determined using a 7-point N_2 adsorption/desorption isotherm collected on the Quantachrome Nova 2000e. Suspensions were weighed and outgassed (or degassed) overnight at approximately 40ºC in pellet cells. The following day, samples were cooled, reweighed, and analyzed for surface area by N_2 adsorption at 77.3 K. The nanoparticle diameter (d_{BET}) of each suspension was calculated using Equation 1, which assumes a cubic particle shape and a hematite density of 5.24 g/cm^3 (Housaindokht & Nakhaei Pour, 2012; Nakhaei Pour et al., 2014).

$$d_{BET} = \frac{6}{\rho A} \times 1000 \quad (1)$$

In this equation, ρ is the density of hematite in g/cm^3 and A is the surface area in m^2/g.

2.4.2. Thermogravimetric Analysis/Differential Scanning Calorimetry (TGA/DSC)

Thermal analyses by TGA/DTG and DSC of hematite suspensions were examined for hydroxylation and phase changes using a Perkin Elmer STA 6000. Samples were heated from 30°C to 800°C at 10°C/min in the presence of nitrogen. Prior to the analysis of these suspensions, a thermogram of an aluminum oxide ceramic crucible was collected as a baseline and subtracted from the thermal data of each sample to remove the effects of heating the crucible. The residual weight percent of hematite at each temperature interval was calculated by

$$\text{wt \%} = \frac{m}{m_0} \times 100 \quad (2)$$

where m is the mass of the sample at a given temperature and m_0 is the initial mass of the sample. DTG was determined by taking the derivative of Equation 1 with respect to temperature every 5°C and is given by

$$\frac{d(wt\%)}{dT} = \frac{(m_2 - m_1)/m_0}{T_2 - T_1} \times 100 \quad (3)$$

where T_1 and T_2 are temperature, and m_2 and m_1 are the masses recorded at T_1 and T_2. A 5-point moving average was applied to these results to remove noise and smooth the curve.

Peak area analysis of nanoparticle suspension DSC results were used to determine enthalpies of dehydroxylation (ΔH_{rxn}). The analyses consisted of finding the area under the curve for peaks in the 150 to 400 °C range by Riemann sum. A baseline was established by determining a slope between two end points of each peak and was used in to determine peak height in the calculations. Hess's Law was used to compare literature values by calculating the ΔH_{rxn} of dehydroxylation for various iron hydroxides from enthalpies of formation (ΔH_f).

2.4.3. Attenuated Total Reflectance-Fourier Transform Infrared Spectroscopy (ATR-FTIR)

A Perkin Elmer Frontier FTIR Spectrometer with a GladiATR attachment fitted with a diamond ATR crystal was used to collect FTIR spectra to characterize hematite nanoparticles from the column experiments. Hematite nanoparticle suspensions were freeze-dried for analysis while hematite-coated sands were air dried in the oven. Each sample spectrum consisted of a background scan followed by four scans over the range of 4000 cm^{-1} to 250 cm^{-1} using a deuterated triglycine sulfate (DTGS) detector.

2.4.4. Ultraviolet-Visible Spectroscopy (UV-Vis)

A Thermo Scientific Evolution 201 ultraviolet-visible (UV-Vis) spectrometer with a dual silicon photodiode detector was used to measure bisulfide in the column effluent according to the methylene blue method by developed by Cline (1969). Two reagents were prepared to measure

bisulfide concentrations in the ranges of 3 to 40 µM and 40 to 250 µM by dissolving N,N-dimethyl-p-phenylenediamine sulfate (Alfa Aesar, 98%) and ferric chloride hexahydrate (VWR) in 500 mL of 50% (v/v) hydrochloric acid (Trace Metal Grade, Fisher Chemical). Standards corresponding to these reagent ranges were diluted from the $Na_2S•9H_2O$ stock solution mentioned in Section 2.2. Both bisulfide standards and diamine reagents were prepared in the anaerobic chamber, and reagents were then stored in amber bottles and refrigerated. Prior to analysis, reagent was added to each sample and standards on the benchtop. The lower concentration reagent was used on the samples eluted with 0.1 mM bisulfide or collected at the beginning of the higher bisulfide concentration experiments, and the higher concentration reagent was added to the remainder of the samples. In some cases, samples were diluted with DDI water in order to be quantified with the available standards. Samples were transferred to cuvettes following the addition of the reagent and analyzed by UV-Vis. The absorbance at approximately 670 nm was used to calculate the concentration of bisulfide using

$$C_{\sum S}=F\ (A-A_b) \tag{4}$$

where $C_{\sum S}$ is the hydrogen sulfide concentration, F is slope calculated from the calibration curve, A is the absorbance of the sample, and A_b is the absorbance of a blank.

2.4.5. Inductively Coupled Plasma-Mass Spectrometry (ICP-MS)

A Thermo Scientific X-Series 2 inductively coupled plasma mass spectrometer (ICP-MS) was used in collision cell technology with kinetic energy discrimination (CCT-KED) mode to measure the concentration of dissolved iron and rubidium in samples. Standards for the calibration curve were prepared for a range of 2 to 60 µg/L from an iron stock solution (prepared from Ultra Scientific 1000 ug/mL Fe in 2% HNO_3) and 2 to 50 µg/L from a rubidium stock (prepared from

Elemental Scientific 1000 ug/mL Rb in 1% HNO_3). Blanks of 5% HNO_3 were analyzed every 12 samples to monitor cross contamination throughout the run.

Effluent samples were transferred into 1 mL microcentrifuge tubes and centrifuged (Fisher Scientific accuSpin Micro 17) at 13.3 rpm x 1000 for 10 minutes to remove any solids from washout or precipitation in the samples. The solution from these tubes was diluted with 5% trace metal nitric acid. Second and third dilutions were done to measure rubidium and iron in samples beyond the calibrant range when analyzing first dilutions. All nitric acid solutions were prepared using DDI (18.2MΩ) water.

2.4.6. Integrated Kinetic Rate Model

A model estimating dissolution-precipitation kinetics was developed based on the elemental analysis of iron by ICP-MS. Equations 5 through 8 are the dissolution and precipitation reactions used in the model and are based on studies by Poulton et al. (2004) and Rickard (1995).

$$Fe_2O_3\,(s) + HS^- + 5H^+ \rightarrow 2Fe^{2+} + S^0 + 3H_2O \quad (5)$$

$$Fe^{2+} + HS^- \rightarrow FeS\,(s) + H^+ \quad (6)$$

$$Fe^{2+} + 2HS^- \rightarrow Fe(HS)_2\,(s) \quad (7)$$

$$Fe(HS)_2\,(s) \rightarrow FeS\,(s) + H_2S \quad (8)$$

The rate of dissolution, R_{Fe}, is given by Equation 9, in which k_{Fe} is the rate constant for iron dissolution, A_0 is the initial surface area in m^2/L, $[HS^-]$ is the bisulfide concentration, and n_1 is the reaction order (Poulton et al. 2004). Equation 10 is the modified R_{FeS} from Rickard (1995), where k_{FeS} is the rate constant for FeS precipitation, [Fe] is the concentration of ferrous iron in solution, and n_2 is the reaction order. Rickard (1995) describes FeS precipitation as a two-step process given by Equations 7 and 8, but a combination of reactions between Equations 6 and 8 is likely to produce

FeS in the column. Based on these equations, n_2 is expected to be between 1 and 2. Using the measured pH values of influent solutions listed in Table 1, the dominant sulfur species is bisulfide in these experiments.

$$R_{Fe} = k_{Fe} A [HS^-]_0^{n_1} \tag{9}$$

$$R_{FeS} = k_{FeS} [Fe] [H_2S]_0^{n_2} \tag{10}$$

The net reaction for dissolved iron in the effluent at time *t* is given by Equation 11, which is the difference between total iron dissolved (Equation 9) and the iron removed from solution through FeS precipitation (Equation 10). In addition to these reaction rates, the rate of surface area loss due to FeS precipitation is given by Equation 11, a modified equation from Rickard (1995) in which k_A is the rate constant for surface area loss. This model assumes first order degradation of surface area due to passivation from precipitation based on physical observations of columns and iron data from column effluent.

$$R_A = \frac{dA}{dt} = -k_A A_0 [HS^-]_0^{n_2} \tag{11}$$

$$A = A_0 e^{-k_A [HS^-]_0^{n_2} t} \tag{12}$$

Integration of Equation 11 results in Equation 12, which was substituted into Equation 13. Steps leading from Equation 13 from Equation 29 are shown below.

$$R_{Fe(net)} = \frac{d[Fe]}{dt} = k_{Fe} A [HS^-]_0^{n_1} - k_{FeS} [Fe] [HS^-]_0^{n_2} \tag{13}$$

$$R_{Fe(net)} = \frac{d[Fe]}{dt} = k_{Fe}A_0 e^{-k_A[HS^-]_0^{n_2}t}[HS^-]_0^{n_1} - k_{FeS}[Fe][HS^-]_0^{n_2} \quad (14)$$

Let,

$$a = k_{Fe}A_0[HS^-]_0^{n_1} \quad (15)$$

$$b = k_A[HS^-]_0^{n_2} \quad (16)$$

$$c = k_{FeS}[HS^-]_0^{n_2} \quad (17)$$

Substitution of a, b, and c (Equations 15 through 17)

$$\frac{d[Fe]}{dt} = ae^{-bt} - c[Fe] \quad (18)$$

$$\frac{d[Fe]}{dt} + c[Fe] = ae^{-bt} \quad (19)$$

$$(e^{ct})\frac{d[Fe]}{dt} + (e^{ct})c[Fe] = (e^{ct})ae^{-bt} \quad (20)$$

$$ce^{ct} = (ce^{ct})' \quad (21)$$

$$(e^{ct})\frac{d[Fe]}{dt} - (ce^{ct})'[Fe] = ae^{(c-b)t} \quad (22)$$

$$(e^{ct})\frac{d[Fe]}{dt} - (ce^{ct})'[Fe] = (e^{ct}[Fe])' \quad (23)$$

$$(e^{ct}[Fe])' = ae^{(c-b)t} \quad (24)$$

$$\int(e^{ct}[Fe])'dt = \int ae^{(c-b)t}\,dt \quad (25)$$

$$e^{ct}[Fe] + C_1 = \int ae^{(c-b)t}\,dt \quad (26)$$

$$[Fe]=\frac{\int ae^{(c-b)t}\,dt-C_1}{e^{ct}} \tag{27}$$

$$[Fe]=\frac{ae^{(c-b)t}}{(c-b)e^{ct}}-\frac{C_1}{e^{ct}} \tag{28}$$

Substituting a, b, and c (Equations 15-17) back into Equation 28 yields

$$[Fe] = -\frac{C_1}{e^{k_{FeS}[HS^-]_0^{n_2}t}}+\frac{k_{Fe}A_0[HS^-]_0^{n_1}}{[HS^-]_0^{n_2}(k_{FeS}-k_A)e^{k_A[HS^-]_0^{n_2}t}} \tag{29}$$

$$[Fe] = -\frac{C_1}{e^{k_{FeS}[HS^-]_0^{n_2}t}}+\frac{k_{Fe}A_0[HS^-]_0^{n_1-n_2}}{(k_{FeS}-k_A)e^{k_A[HS^-]_0^{n_2}t}} \tag{30}$$

$$C_1^*=\frac{k_{Fe}A_0[H_2S]_0^{n_1-n_2}}{k_{FeS}-k_A} \tag{31}$$

Equation 30 is used in the model to calculate rate constants by finding the minimum value of the sum of squares based on the variance between collected data and model results. C_1 is an integration constant, and C_1* in Equation 31 is the expected value for the constant C_1 when t=0 and is used as a benchmark to constrain C_1 and the model.

CHAPTER 3

RESULTS

3.1. Characterization of Hematite Nanoparticles

3.1.1 Particle Size by BET Surface Area Analysis

BET surface area analysis shows an order of magnitude difference between small and large particle diameters. The calculated diameters of both particles using Equation 1 are listed in Table 2. Small particles have an approximate diameter of 7.1 nm, and the large particles are approximately 104 nm in diameter. The small particle diameter is in close agreement with the 7.3 nm diameter measured by Madden et al. (2006), and TEM results in their study show that the particle shape from this synthesis was pseudo-hexagonal rather than spherical (Madden et al., 2006). Schwertmann and Cornell (2000) reported a particle diameter of 30 to 50 nm for the large particle synthesis, which is much lower than the particle size calculated here through BET results. The order of magnitude difference in particle diameter still confirms that the synthesis methods produce hematite nanoparticles of significantly different sizes.

Table 2. Approximate particle diameter calculated from BET surface area

Particle Size	A_{BET} (m^2/g)	d_{BET} (nm)
Small	161.089	7.1
Large	10.979	104

3.1.2. Thermal Analysis by TGA/DSC/DTG

Thermal analysis of hematite nanoparticles showed weight loss and energetic changes caused by water loss. Previous studies have reported that adsorbed, or surface, water is released below 150°C, while structural water leaves at temperatures ranging from 150°C to 400°C (Darezereshki, 2011; Gualtieri & Venturelli, 1999; Michel, Ehm, Liu, et al., 2007; Yao & Millero, 1996). Figure 2 shows the residual weight percent of each hematite sample over the temperature range, while percentages and proportions attributed to surface and structural water in each sample are given in Table 3. The percentage mass loss was significantly larger for small particles than for large particles. The total amount of water released between 30°C and 400°C was 16.86% for small particles and 2.05% for large particles. The weight percent lost from the removal of surface water was 9.25% for small particles and 0.84% for large particles. The weight percent attributed to structural water was 7.61% for small particles and 1.21% for large particles. The percentages of surface and structural water were higher for the small particles and make up a larger portion of their composition. Using BET surface areas from Table 2, structural hydration at the surface was 47 mg/m^2 for small particles and 110 mg/m^2 for large particles. Despite having a lower percent weight loss in TGA results, large particles have more structural water at the surface relative to small particles when normalized to available surface area. These results indicate that the particles exhibit large differences in water content due to particle size and specific surface area.

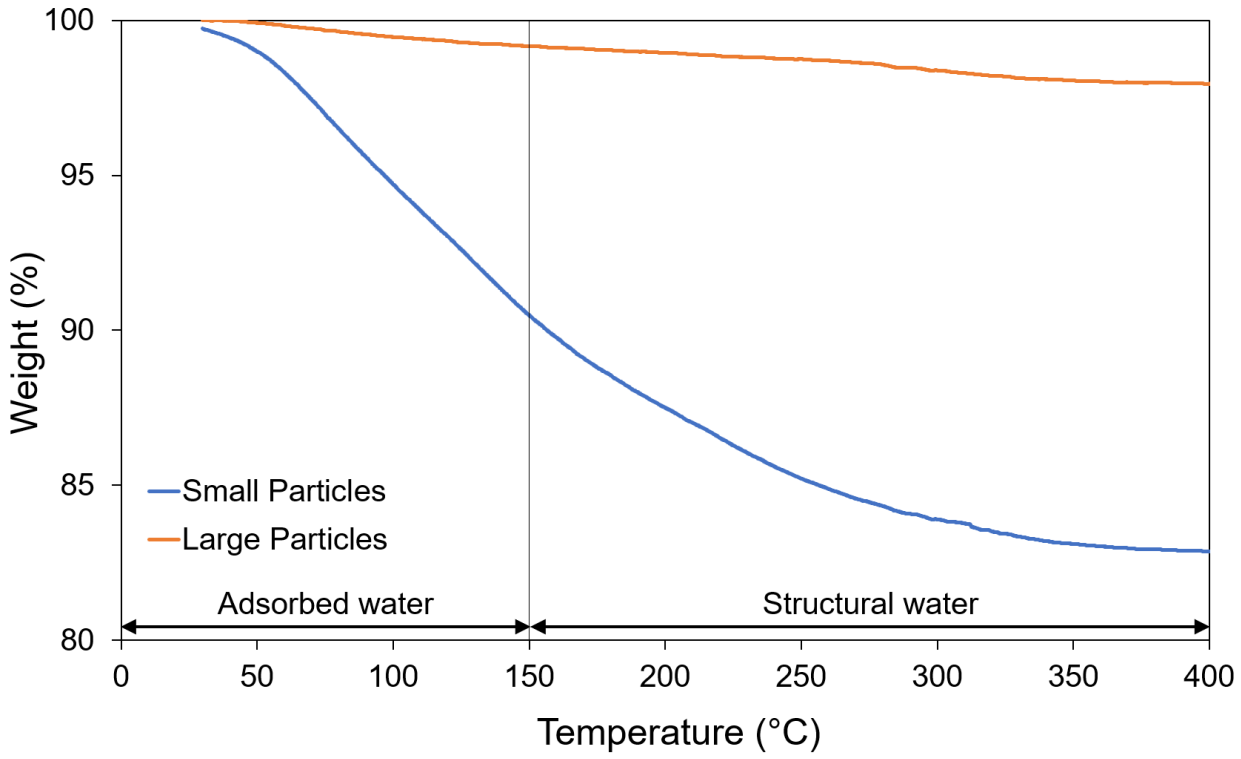

Figure 2. TGA thermogram for small and large hematite nanoparticles. TGA thermogram for small (blue) and large (orange) hematite nanoparticles heated from 30°C to 400°C. Weight loss below 150°C is attributed to adsorbed water, while weight loss between 150°C and 400°C is associated with structural water.

Table 3. Weight percent attributed to adsorbed water and hydroxyl groups as hematite nanoparticles are heated up to 400°C

Particle Size	Total Percent Weight loss (wt.%) 30-400 ˚C	Percent Weight Loss from Surface Water (wt.%) 30-150 ˚C	Percent Weight Loss from Hydroxyl Groups (wt.%) 150-400 ˚C	Structural Hydration (mg/m^2)
Small	16.86	9.25	7.61	47
Large	2.05	0.84	1.21	110

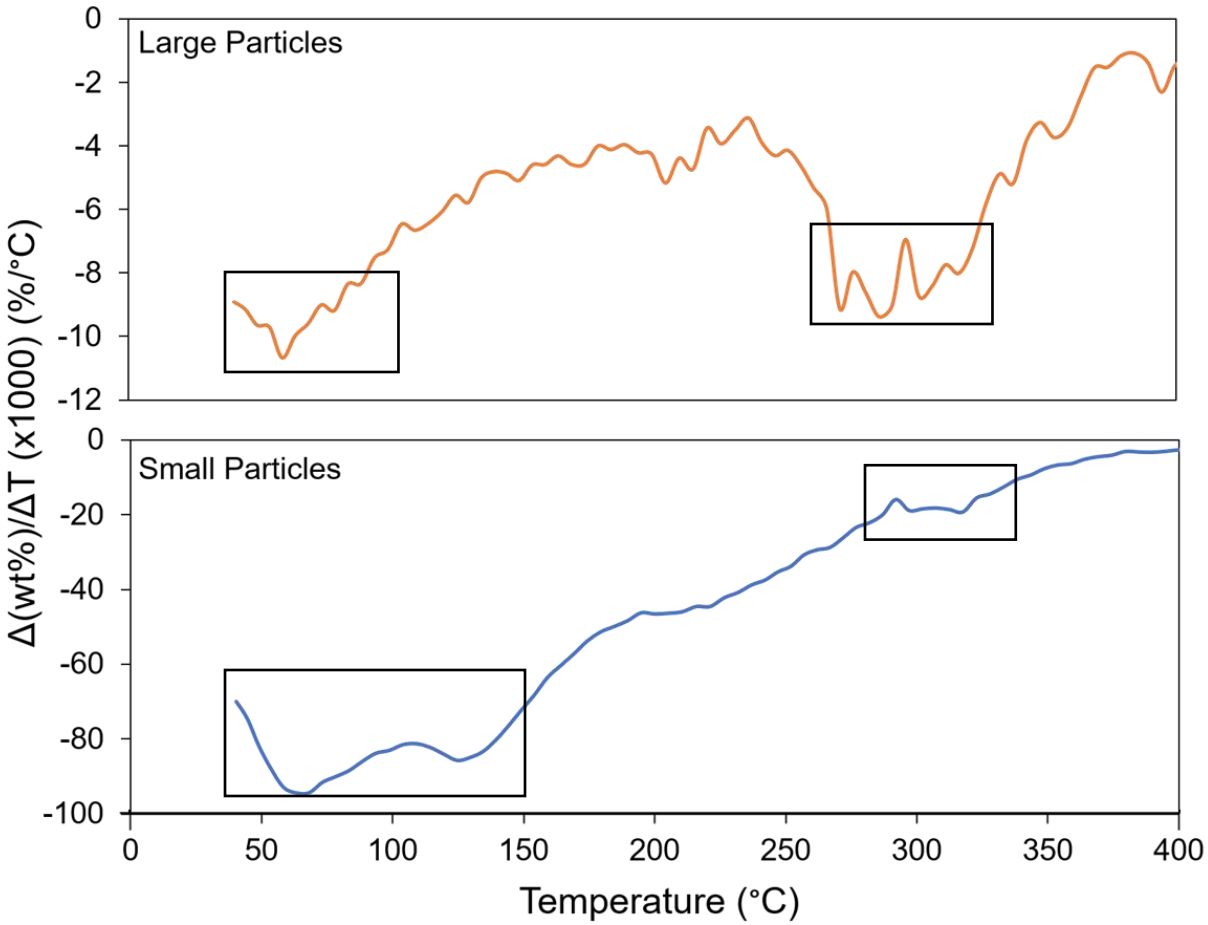

Figure 3. Smoothed DTG thermograms for large (top) and small (bottom) particles heated from 30°C to 400°C. Endothermic peaks generally correspond to regions associated with adsorbed water surface hydroxylation observed in TGA (Figure 2) and DSC (Figure 4) results. Development of smoothed DTG plots consisted of subsampling from the results by 5°C and was followed by a 5-point boxcar smoothing.

DTG and DSC thermograms further exhibit peaks in the 30°C to 400°C region associated with the release of surface and structural water. DTG for small particles in Figure 3 show a large well containing two endothermic peaks at approximately 68°C and 124°C and a low intensity peak between 250°C and 300°C. Endothermic peaks between 250°C and 350°C are present for large particles, but the size and intensity of these peaks were much smaller than those observed for small particles. The peaks at approximately 58°C, 205°C, and 215°C could be insignificant due to their small size and low intensity. Noise in the DTG plot for large particles is greater due to the order

of magnitude difference in the derivative values relative to the small particles. The DSC plot in Figure 4 shows an endothermic peak at approximately 250°C for both particle sizes and a second endothermic peak at approximately 314°C for small particles only. These peaks occur in the range known for the removal of hydroxides and is typically associated with the dehydration of goethite (Darezereshki, 2011; Gualtieri & Venturelli, 1999; Yao & Millero, 1996). DTG and DSC results are consistent with weight loss measurements from TGA and indicate the presence of surface and structural water in the designated ranges.

Further analysis of DSC and DTG thermograms and comparison of these data to TGA results are useful in understanding size-dependent differences caused by dehydration of structural water. Enthalpies of reaction in the 150 to 400°C for the dehydration of hematite nanoparticles, or ΔH_{rxn}, are 53.8 KJ/mol for small particles and 103.2 KJ/mol for large particles. Enthalpies of reaction for nanoparticles were compared to literature values for iron hydroxides by calculating ΔH_{rxn} from Hess's Law. Table 4 shows that the ΔH_{rxn} values calculated for the hematite suspensions, where small particles are in close agreement with goethite (53.4 KJ/mol) and large particles are close to ferrihydrite (109 KJ/mol) dehydroxylation. However, these enthalpies may differ because the literature values were measured at STP, while DSC data reported in this study were measured over a range of temperatures. Also, the formula for ferrihydrite used in the calculation refers to often used hydrous ferric oxide rather than the formula given by Michel (2007). These data further indicate that the hematite nanoparticles have an iron hydroxide character observed in TGA results.

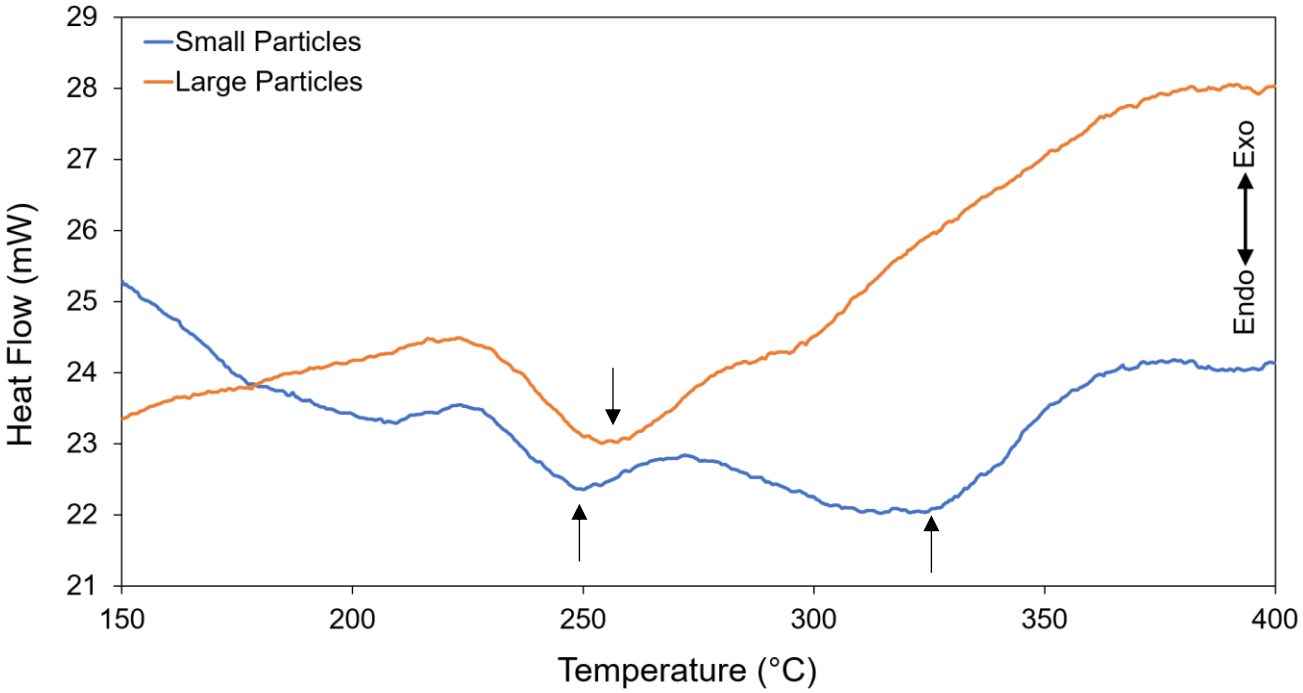

Figure 4. DSC thermograms for small and large particles heated from 150°C to 400°C. Peaks in this region are a result of the removal of structural water consistent with dehydration.

Table 4. Calculated ΔH_{rxn} (KJ/mol) of iron (oxyhydr)oxides

	ΔH_f (KJ/mol)	Reaction	ΔH_{rxn}* (KJ/mol)	Source
Small Particles		$Fe_2O_{(3-x/2)}(OH)_x = Fe_2O_3+xH_2O$	53.8	
Large Particles		$Fe_2O_{(3-x/2)}(OH)_x = Fe_2O_3+xH_2O$	103.2	
		Literature Values		
Goethite	-560.7	$2FeOOH = Fe_2O_3 + H_2O$	53.4	(Majzlan et al., 2003)
Lepidocrocite	-7.19.4	$2FeOOH = Fe_2O_3 + H_2O$	30.8	(Majzlan et al., 2003)
Akageneite	-554.7	$2FeOOH = Fe_2O_3 + H_2O$	41.4	(Navrotsky et al., 2008)
Ferrihydrite	-830.3	$2Fe(OH)_3 = Fe_2O_3 + 3H_2O$	109	(Navrotsky et al., 2008)

*Values used for hematite and water in the calculations: ΔH_f (Fe_2O_3) = -826.2 KJ/mol and ΔH_f (H_2O vapor) = -241.8 KJ/mol. Values are from USGS Bulletin 2131 (1995).

3.1.3. ATR-FTIR

FTIR spectra consist of bands associated with Fe-O and O-H bonds for hematite nanoparticles. Figures 5 and 6 are FTIR spectra of small and large particles for the ranges of 800 cm^{-1} to 300 cm^{-1} and 1800 cm^{-1} to 800 cm^{-1}, respectively. Table 5 lists the bands identified from these spectra and band assignments according to literature. The spectrum for large particles in Figure 5 exhibits two absorption peaks at approximately 441 cm^{-1} and 524 cm^{-1} that can be assigned to the stretching of Fe-O bonds (Chernyshova et al., 2007; El Afifi et al., 2016; Tadic et al., 2019). However, Fe-O bonds in small particles absorb energy in a diffusive manner, peaks are not discernible and cannot be assigned a band position. The large particle spectrum also has a band at 909 cm^{-1} that corresponds to the Fe-O-H bending mode found in goethite (Ruan et al., 2001; Xiao et al., 2017; Zamiri et al., 2014). The frequency band at 1635 cm^{-1} in the small particle spectrum is assigned to the O-H bending mode for water and related to the presence of surface water (Apte et al., 2007; Darezereshki, 2011; Nasrazadani, 1997; Seehra et al., 2004). The low intensity bands at 1353 cm^{-1} and 1472 cm^{-1} could be assigned to bending modes for Fe-O-H and Fe-O observed in goethite and ferrihydrite IR spectra (Nasrazadani, 1997; Rout et al., 2012; Seehra et al., 2004). Spectra for both particles exhibit a broad, low intensity band between 3300 and 3350 cm^{-1}, which is close to the O-H stretching mode caused by the adsorption of water (Darezereshki, 2011; Seehra et al., 2004; Walter et al., 2001). FTIR results further confirm the presence of adsorbed and structural water observed in thermal analysis.

Table 5. Assignment of absorption bands from FTIR spectra for hematite nanoparticles

Absorption (cm^{-1})	Functional Group	Absorption Bands from literature (cm^{-1})	Reference
441	Fe-O stretching mode	460, 430	(Chernyshova et al., 2007; Tadic et al., 2019)
524	Fe-O stretching mode	537, 515	(El Afifi et al., 2016; Tadic et al., 2019)
909	Fe-O-H bending mode	890, 900	(Ruan et al., 2001; Xiao et al., 2017; Zamiri et al., 2014)
1353	Fe-O-H bending mode	1365, 1389, 1392	(Nasrazadani, 1997; Rout et al., 2012; Seehra et al., 2004)
1472	Fe-O bending mode	1493, 1572	(Rout et al., 2012; Seehra et al., 2004)
1635	O-H bending mode	1630, 1637	(Apte et al., 2007; Darezereshki, 2011)
3315	O-H stretching mode	3423, 3400, 3440	(Darezereshki, 2011; Seehra et al., 2004; Walter et al., 2001)
3354	O-H stretching mode	3423, 3400, 3440	(Darezereshki, 2011; Seehra et al., 2004; Walter et al., 2001)

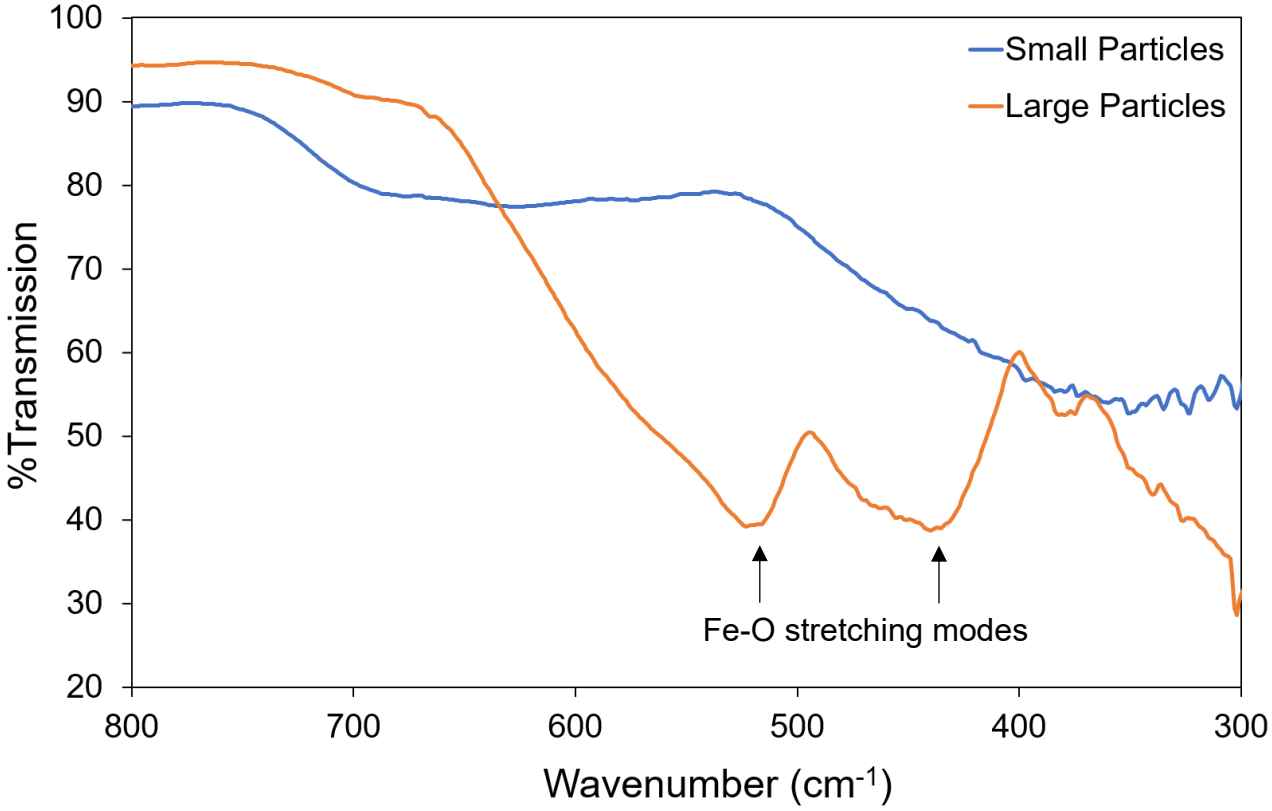

Figure 5. FTIR spectra for small (blue) and large (orange) hematite nanoparticles from 800 cm^{-1} to 300 cm^{-1}. Absorption bands in this region correspond to Fe-O stretching modes for iron oxides.

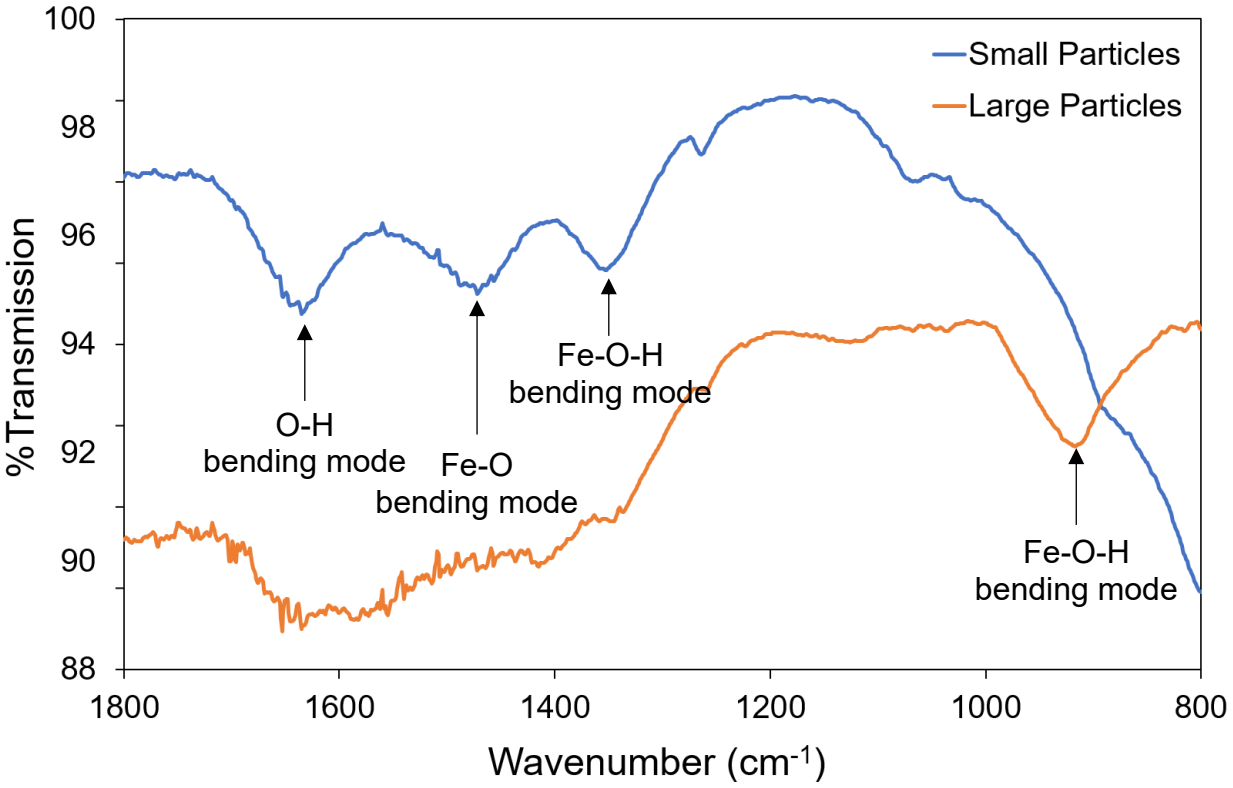

Figure 6. FTIR spectra for small (blue) and large (orange) hematite nanoparticles from 1800 cm^{-1} to 800 cm^{-1}. Absorption bands in this region are associated with structural water or Fe-OH bonds characteristic of iron hydroxides.

3.2. Column Experiments

3.2.1 ICP-MS Results

ICP-MS iron data demonstrate differences in ferrous iron concentrations, a result of reductive dissolution of hematite nanoparticles, in column effluent across particle size and bisulfide concentrations. In all experiments, breakthrough of ferrous iron in the effluent occurred within 20 minutes of reaction. Figures 7 and 8 demonstrate release of ferrous iron concentrations in column effluent over time. Small particles with 0.1 mM bisulfide (Figure 7A) showed maximum dissolved iron of approximately 0.3 µM in solution within the first 12 minutes of reaction and declined to baseline levels of 0.1 µM or less. Large particles exposed to 0.1 mM bisulfide (Figure 8A) exhibited higher iron release throughout the experiment, with concentrations ranging from 0.6

and 0.8 μM between 100 and 150 minutes of reaction and declining to 0.2 μM by the end of the run.

Small particles eluted with 1 mM bisulfide resulted in two peaks. Figure 7C shows a peak occurring in the first 50 minutes of the experiment with maximum dissolved iron concentration of approximately 0.75 μM. A second peak occurs between 200 and 250 minutes with iron in the effluent reaching 1.5 μM. Large particles released iron into solution almost linearly at 1 mM bisulfide (Figure 8C), with maximum iron release of approximately 4 μM occurring by the end of the experiment. Similar to the 0.1 bisulfide experiments, large particles had higher ferrous iron concentrations in solution than measured in small particles.

Both particle sizes showed maximum iron release with the first 20 minutes of reaction when reacted with 10 mM bisulfide, and ferrous iron concentrations declined over the course of each reaction. Maximum iron concentrations were between 25 and 30 μM for small particles (Figure 7E) and between 5 and 10 μM for large particles (Figure 8E). Unlike the 0.1 and 1 μM bisulfide column runs, iron release is greater for small particles.

Results for non-reactive breakthrough of rubidium are presented in Appendix C for all columns.

3.2.2 UV-Vis Spectroscopy Results

Analysis of bisulfide in the column effluent by UV-Vis showed that smaller particles had lower bisulfide in solution relative to large particles for all three concentrations used in the experiments. Effluent from reaction between small particles and 0.1 mM bisulfide (Figure 7B) contained little to no bisulfide throughout the run. Between 15 and 35 μM of bisulfide were measured in solution for large particles at 0.1 mM bisulfide (Figure 8B), and concentrations increased as the experiment progressed. Small particles contained between 200 and 400 μM

bisulfide in the effluent during reaction with 1 mM bisulfide (Figure 7D). Large particles exhibited a similar trend and concentration of bisulfide in the effluent (Figure 8D), but these samples had partially oxidized prior to reagent addition and analysis. Bisulfide concentrations in large particle columns are expected to be higher than small particles. Small particle effluent from the 10 mM bisulfide experiment (Figure 7F) contained between 2000 and 10000 μM bisulfide in the samples. Effluent concentrations did not exhibit the gradual increase in concentration observed at lower bisulfide concentrations. Nearly all effluent samples from the large particles reaction with 10 mM bisulfide contained approximately 10000 μM bisulfide (Figure 8F).

3.2.3 Mineral Transformations

Figures 9 and 10 show that mineral transformations occurred in the small particles eluted with 1 and 10 mM bisulfide and in large particles reacted with 10 mM bisulfide. Small particles reacted with 1 mM bisulfide partially transformed from yellow to black solids approximately 5 to 10 cm from the inlet. The entire column of small particles eluted with 10 mM bisulfide transformed by 177 minutes or 200 mL of collected column effluent. Only large particles eluted with 10 mM bisulfide partially transformed between 2 and 10 cm from the inlet. The black precipitate forming in the column is likely to be disordered mackinawite (Rickard, 1995; Saalfield & Bostick, 2009; Wolthers et al., 2005).

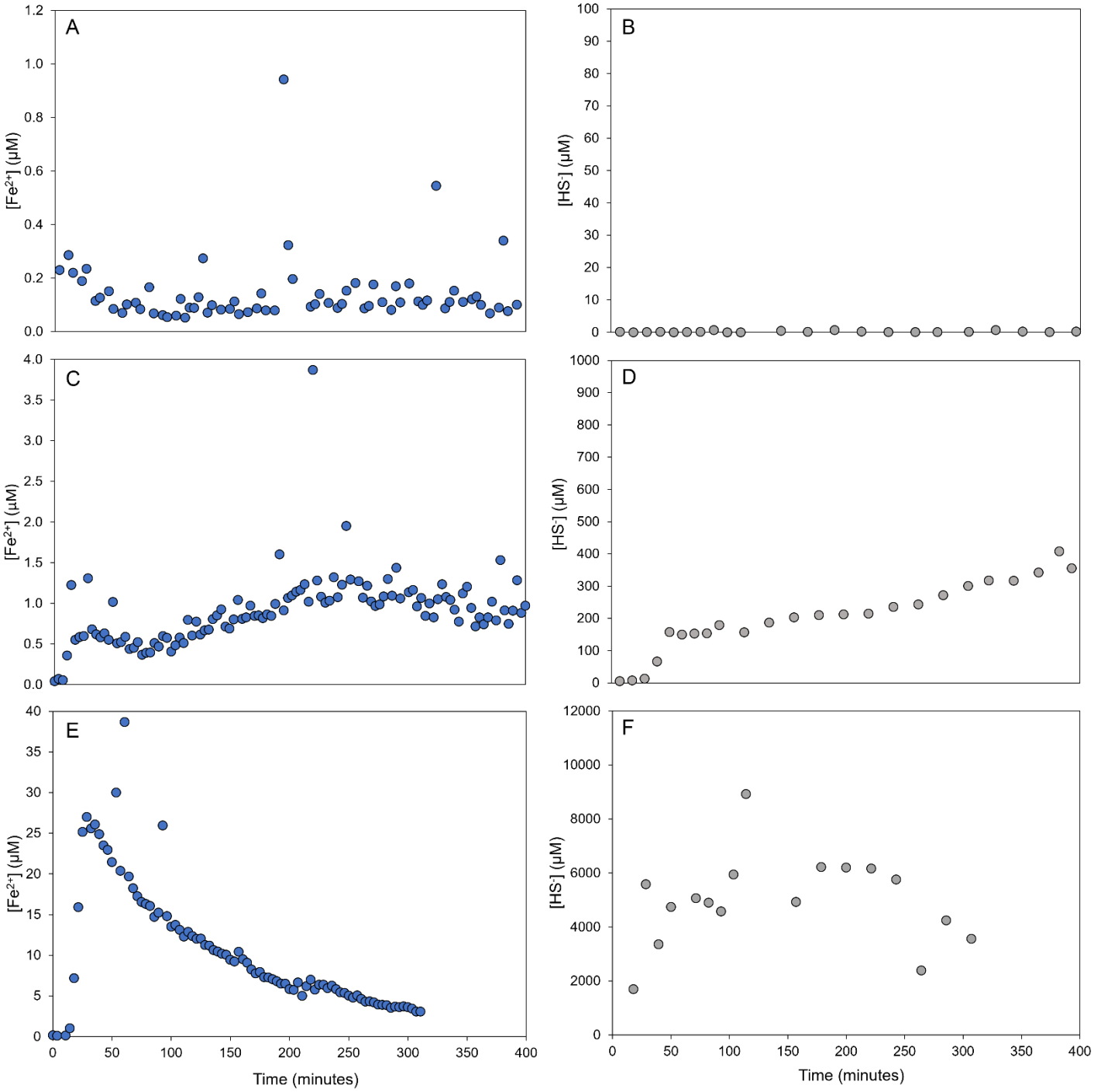

Figure 7. Ferrous iron (left) and bisulfide (right) release in column effluent for small particles eluted with 0.1 mM (A and B), 1 mM (C and D), and 10 mM (E and F) bisulfide.

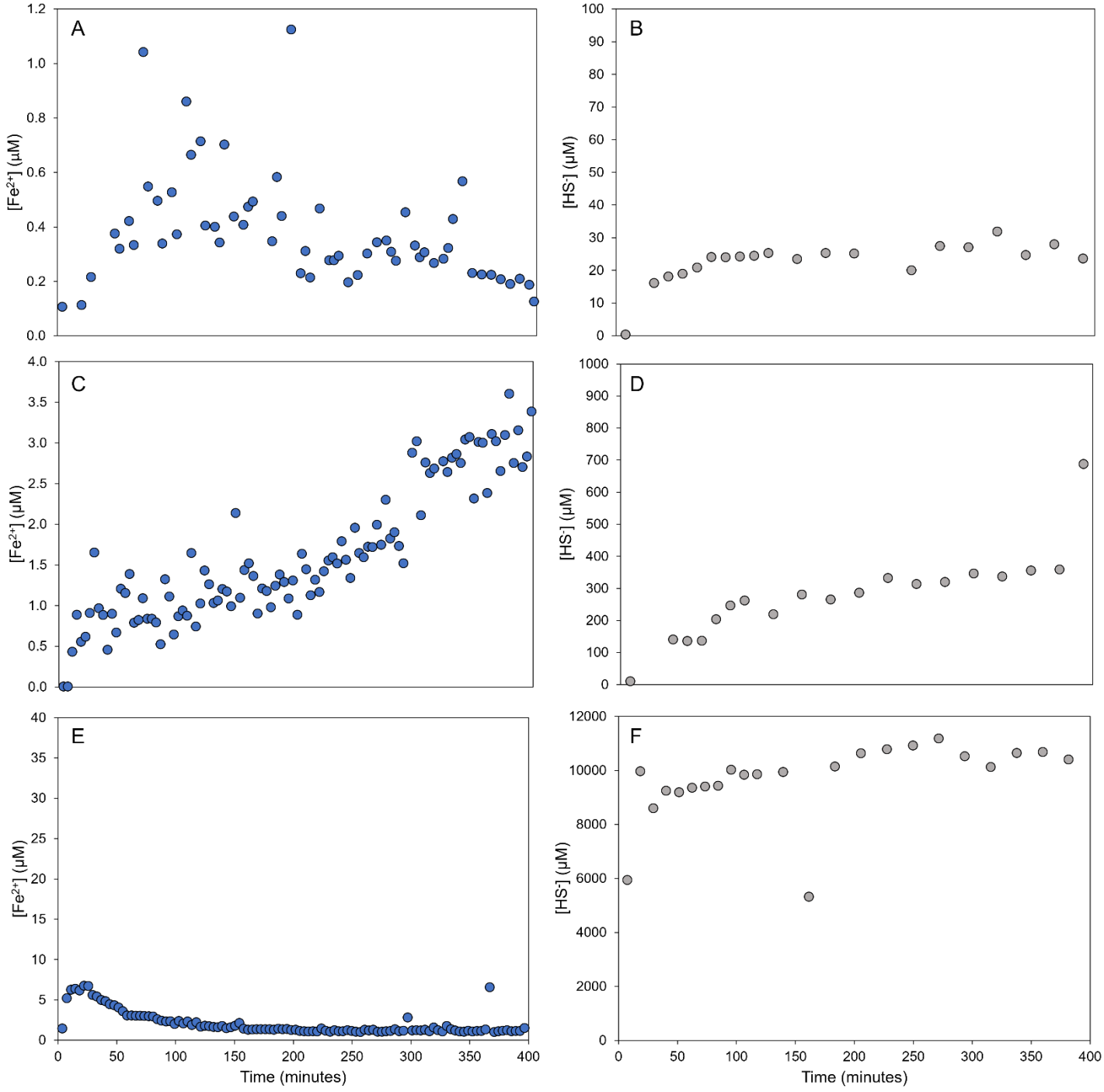

Figure 8. Ferrous iron (left) and bisulfide (right) release in column effluent for large particles eluted with 0.1 mM (A and B), 1 mM (C and D), and 10 mM (E and F) bisulfide.

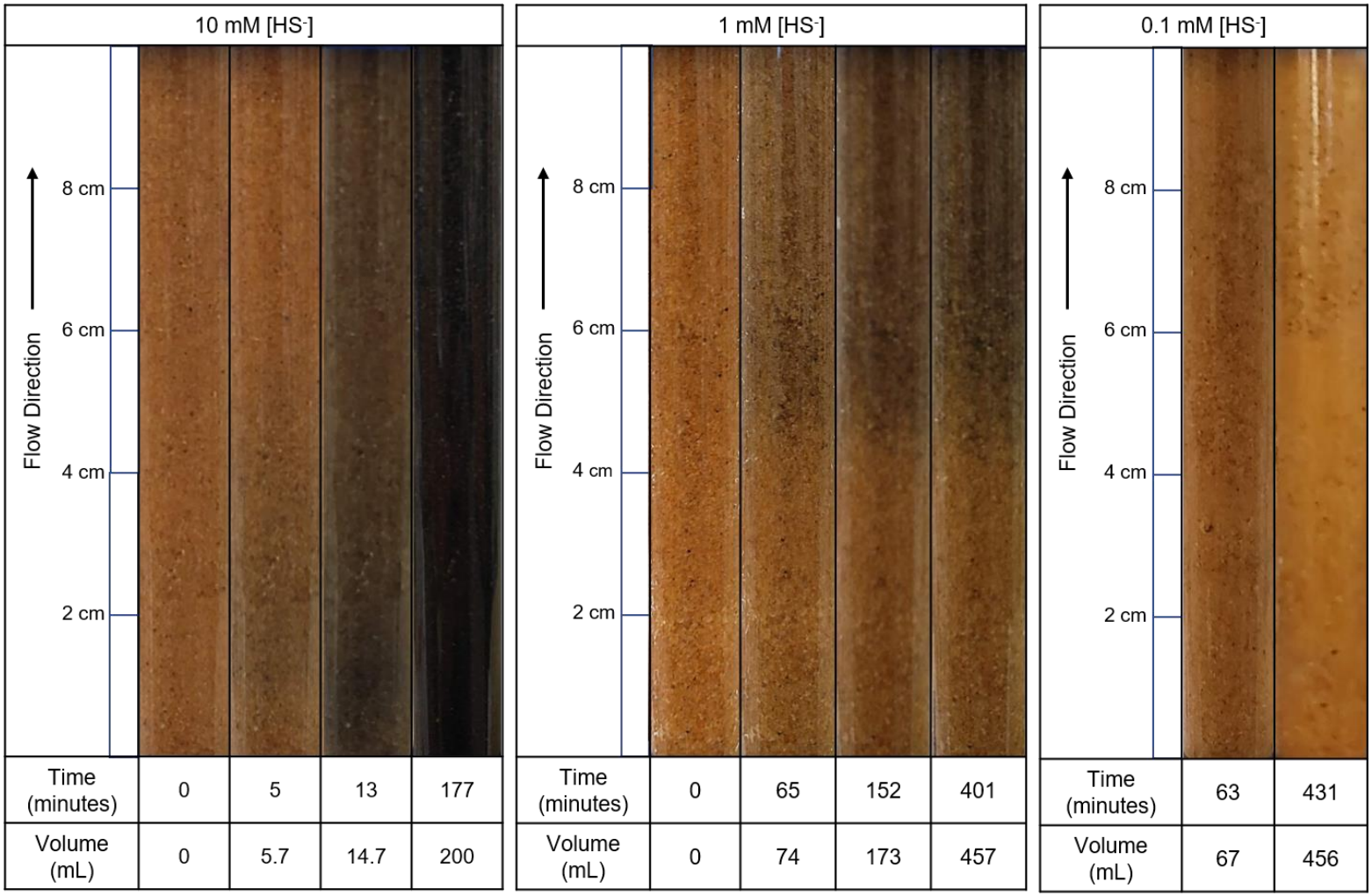

Figure 9. Physical changes in the small particle columns for the 0.1, 1, and 10 mM bisulfide concentrations. Darkening of solids within the column is associated with FeS precipitation. Approximate distances from the inlet are given on the on the left of each bisulfide experiment.

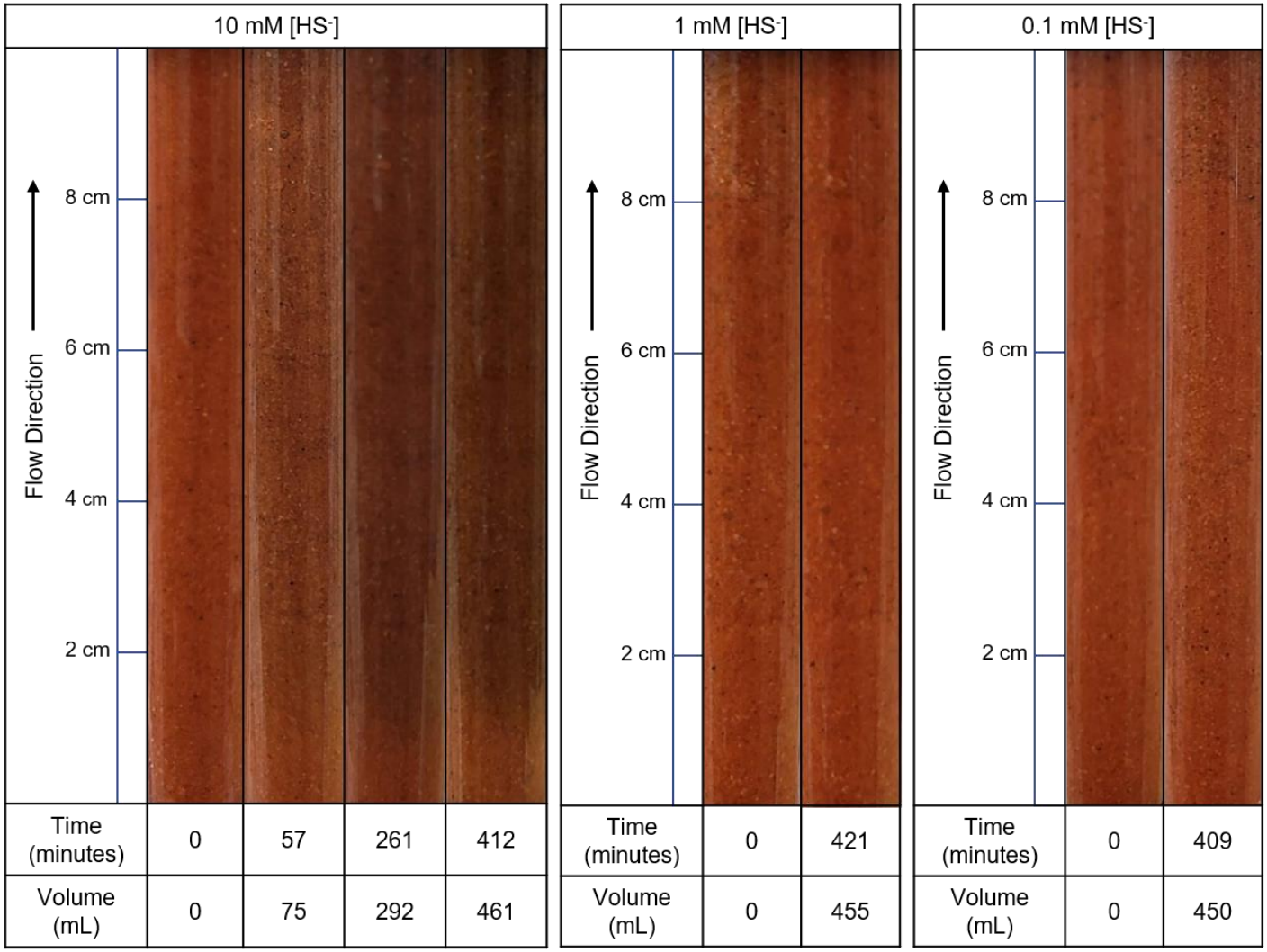

Figure 10. Physical changes in the large particle columns for the 0.1, 1, and 10 mM bisulfide concentrations. Darkening of solids within the column is associated with FeS precipitation. Approximate distances from the inlet are given on the on the left of each bisulfide experiment.

CHAPTER 4

DISCUSSION

4.1. Hematite Nanoparticle Characterization

Solid-phase characterization demonstrates differences in the physical properties of the nanoparticles. BET results show an order of magnitude difference in particle size between the two suspensions. Non-discernible or low intensity bands present in the IR spectra for small particles suggest low crystallinity or disorder caused by a decreasing particle size (Chernyshova et al., 2007). DSC results for small particles have broad, less defined peaks than in large particles.

The synthesis of solid-phase characterization results indicate that both hematite suspensions have some iron hydroxide character at the nanoparticle surface. O-H and Fe-O-H bands are present for both particles in FTIR-ATR spectra. Thermal data agree with these results, and based on enthalpies, variable intensities, and directionality of (endothermic) peaks observed in DSC, water loss between 150 and 400ºC is identified as dehydroxylation at the hematite nanoparticle surface typically found in goethite or ferrihydrite. Large particles have a lower weight percent of hydroxyls (2.05%) relative to small particles (16.86%). However, large particles have greater hydroxylation per surface area (110 mg/m^2 versus 47 mg/m^2). The enthalpies for dehydroxylation from DSC agree with these results, where ΔH_{rxn} is 103.2 KJ/mol for large particles

and 53.8 KJ/mol for small particles. The combined results show that while small particles have very high specific surface area and hydroxyl content paired with low crystallinity similar to ferrihydrite, large particles have more hydroxyls on an area normalized basis. Chernyshova et al., (2007) found that hydroxyls provide stability to nanoparticles and inhibit phase transitions often observed with decreasing particle size and can be important beyond a critical particle size. These differences in particle surface character due to scale influence the reaction mechanism of sulfidation in advective flow experiments.

4.2. Advective Flow Experiments

Ferrous iron concentrations increase with bisulfide concentration, but iron concentrations and trends vary across all experiments (Figures 7 and 8). Ferrous iron release is highest in small particles reacting with 10 mM sulfide, and 1 mM and 0.1 mM bisulfide have lower concentrations of iron in the effluent relative to large particles. In the reaction between small particles and 1 mM bisulfide (Figure 7C), the first peak could be associated with reductive dissolution of Fe, and based on Figure 9, the second peak could coincide with the color change observed in the upper half of the column. Based on the black color of the solids and the column conditions, the hematite could have transformed to FeS such as disordered mackinawite (Rickard, 1995; Saalfield & Bostick, 2009; Wolthers et al., 2005). The second peak has a higher concentration and duration, and images of the column reveal incomplete precipitation relative to the 10 mM column experiment. Large particles show increasing iron concentrations in the effluent and no color change over the course of the run (Figure 8C), suggesting that reductive dissolution of iron is the main process occurring in the column. Both particle sizes show a similar shape and trend in iron release over time. The small particle column changes color entirely, while solids transform partially in the large column. The 10 mM columns (Figures 7E and 8E) show the expected trend of reductive dissolution of

hematite releasing maximum concentrations of iron at the beginning of each experiment, followed by a decline as precipitation occurs. Iron concentrations are also lower for large particles at this concentration, which contrasts the results for the 0.1 and 1 mM experiments, but this could indicate that more of the reduced iron remained in the column through FeS precipitation. Due to the low concentrations of iron release, the 0.1 mM bisulfide reaction data for iron (Figure 7A and 8A) act as a baseline.

4.3. Integrated Kinetic Rate Model

Modeling of the column experiments presented in the previous chapter produced fits across all ferrous iron plots versus time (Figures 7 and 8). Model results are listed in Table 6 and fits are shown in Figures 11 and 12. Nearly all of the parameters manipulated in the model are consistent across the various sulfide concentration experiments within small standard deviations. The exception is the kinetic constant for iron reductive dissolution. The k_{Fe} for both particle sizes differs by just less than two orders of magnitude, with the $\log k_{Fe}$ for large particles being -6.2±0.2 and -7.9±0.5 for small particles. These values indicate that large particles have a faster dissolution rate. The greater hydroxylation per surface area (110 mg/m^2) could be causing faster reaction rates, resulting in higher concentrations of ferrous iron in both the 0.1 mM and 1 mM bisulfide experiments (relative to small particles. Greater hydroxylation could represent a lower degree of hematite crystallinity and more iron hydroxide character. Iron hydroxides like goethite and ferrihydrite promote faster solubility than hematite.

In comparison to log k_{Fe} values measured by Poulton et al. (2004), the rate constant falls between hydrous ferrous oxide (-5.1) and hematite (-6.4), while the small particles are closer to goethite (-7.1). The $\log k_{FeS}$ values calculated by Rickard (1995) were between approximately 2 to 7, but the values reported in this study fall slightly below this range. This difference could be due

to the variable iron concentration used in this study, whereas the Fe(II) concentration was constant in Rickard (1995). Based on the chemical reactions that may be occurring in the column experiments, the n_2 value is closer to reaction order of 1 than 2. The n_1 value from Poulton et al. (2004) is within range of value calculated by the authors in their experiments. The parameters stagnant across both particle sizes suggest that reaction order, bisulfide concentration, surface area, and FeS precipitation may not influence dissolution rates. Parameter values for each experiment are shown in the Appendix.

Table 6. Average values of parameters generated through kinetic modeling.

	Small Particles		Large Particles	
$\log k_{Fe}$	-7.9	±0.5	-6.2	±0.2
$\log k_{FeS}$	1.5	±0.2	1.4	±0.2
$\log k_A$	-2.7	±0.4	-2.5	±0.5
$\log [HS^-]_0$	3.0	±1.0	3.0	±1.0
n_1	0.6	±0.1	0.6	±0.0
n_2	1.1	±0.2	1.0	±0.1
$\log(-C_1)$	-5.0	±0.6	-5.2	±0.2
$\log(-C_1^*)$	-5.0	±0.6	-5.1	±0.2

Despite these results, differences are observed between the experiment and model in Figures 11 and 12. The largest variation appears for both particles sizes with the 1 mM bisulfide. These deviations indicate that the model is not capturing a process or accounting for a variable influencing iron release. One factor that could affect these reactions is pH. While influent pH was fixed between 7.5 and 8.5 at the beginning of all experiments, it was not monitored over the course of the experiment. Monitoring both influent and effluent pH could determine whether pH is

conservative while interacting with the coated sand or if oxidation is occurring somewhere in the apparatus.

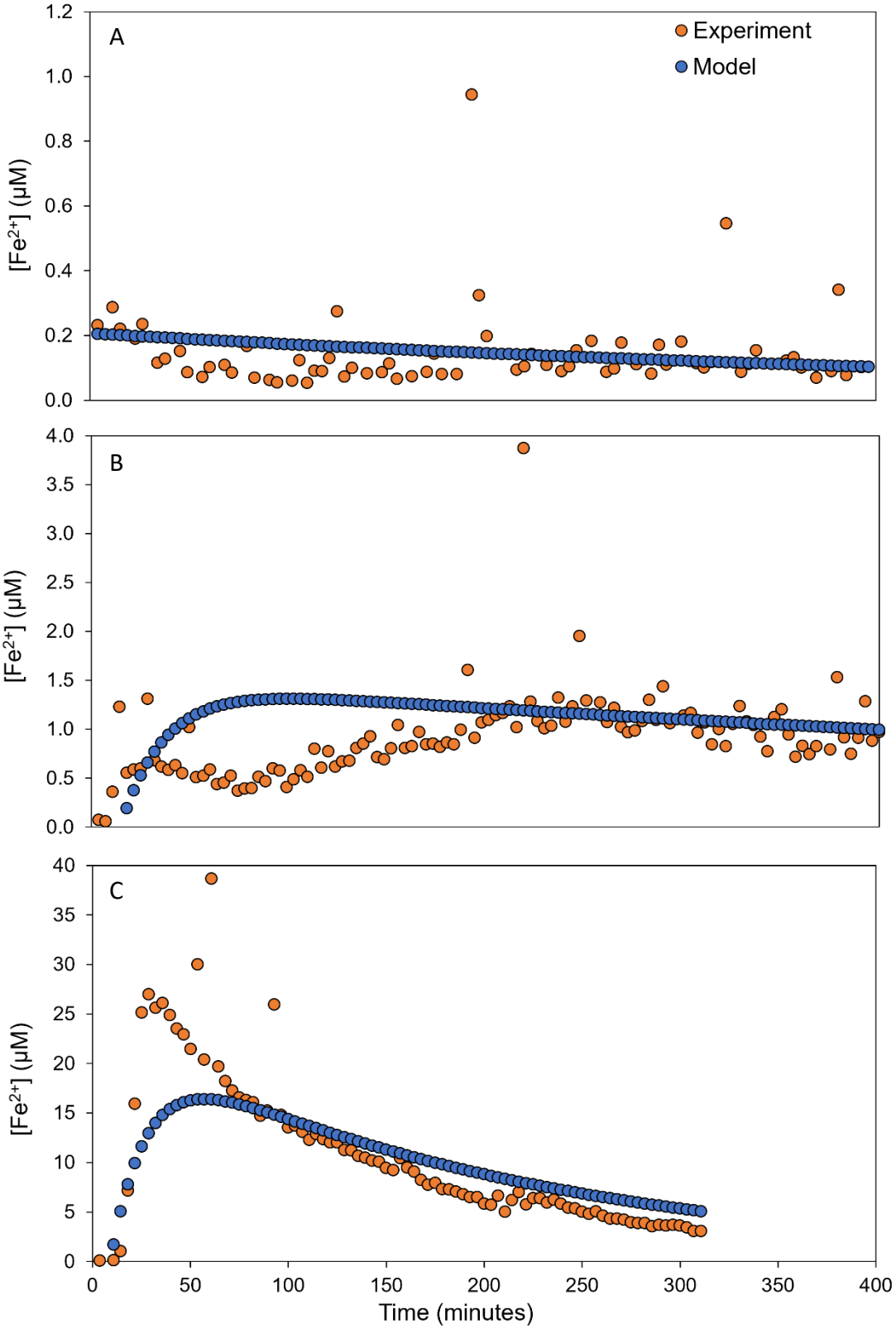

Figure 11. Model fits (blue) relative to experimental data for ferrous iron (orange) in effluent for small particles eluted with 0.1 mM (A), 1 mM (B), and 10 mM (C) bisulfide.

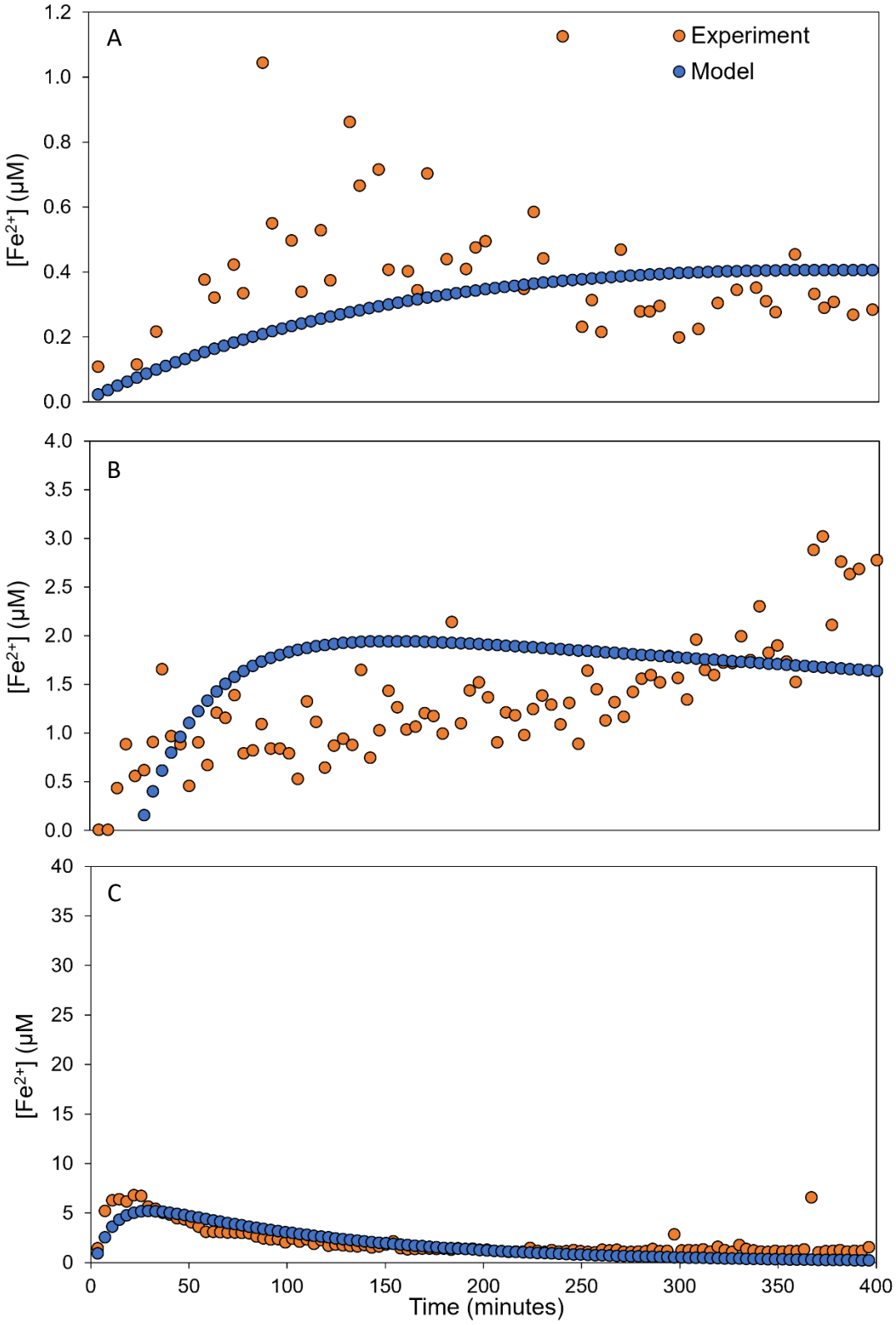

Figure 12. Model fits (blue) relative to experimental data for ferrous iron (orange) in effluent for larger particles eluted with 0.1 mM (A), 1 mM (B), and 10 mM (C) bisulfide.

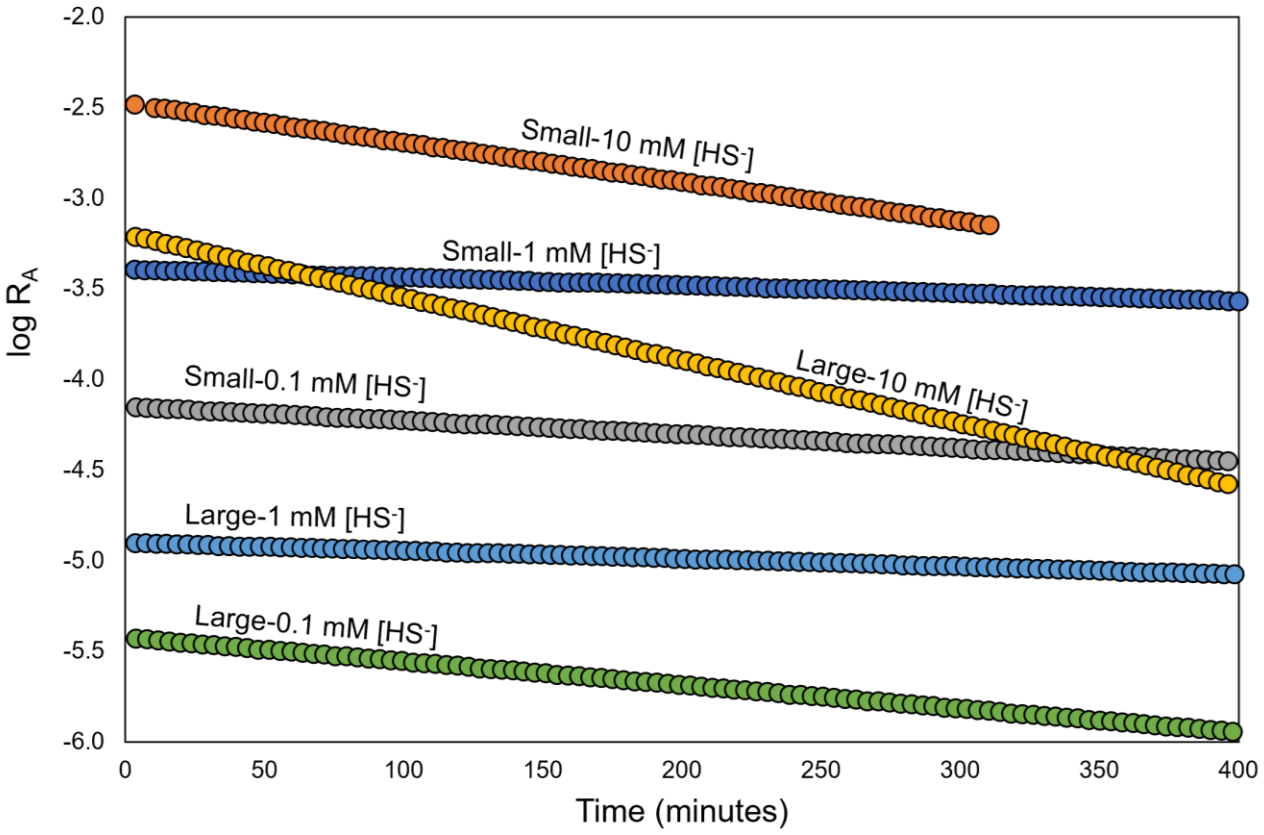

Figure 13. The logarithm of the reaction rate for surface area loss (log R_A) as a function of time.

The modeling results discussed above only explain iron dissolution results and not the trends observed in FeS precipitation. Figure 13 shows the log R_A for surface area loss as a function of time for all experiments. The plot shows that the 10 mM reactions have the sharpest decline in reactive surface area compared to the other columns, and the three experiments with FeS precipitation have the highest initial R_A values and maintain the fastest precipitation rates over the majority of the reaction period. These results suggest that FeS precipitation is dependent on the initial bisulfide concentration and surface area.

The advective flow experiments and model results deviate from the expectation that small particles are more reactive and likely to have faster dissolution and precipitation kinetics. However, this study has shown that surface area alone cannot be only factor influencing these

reactions, and the mechanism needs to be taken into account. Here, an optimization issue arises during surface mediated reactions for small particles. Reaction kinetics may differ from expected trends if the small particles are below a critical size and undergo significant changes in their properties.

CHAPTER 5

CONCLUSION

This study shows that particle size influences reductive dissolution and precipitation mechanisms during the sulfidation of hematite nanoparticles under advective flow conditions.

Characterization of synthetic nanoparticles with approximate diameters of 7.1 nm and 104 nm show that both suspensions had hydroxides present at the particle surface. The ΔH_{rxn} values and ATR-FTIR results confirm the presence of hydroxyls at the surface of these suspensions. Hydroxylation per surface area was higher for large particles even through small particles had a higher total hydroxide content. Hydroxylation appears to be an important factor in the reactivity of these particles.

The model developed to estimate rate constants and reaction orders for the advective flow experiments shows that large particles have faster reaction rates than small particles. The greater hydroxylation per surface area appears to influence dissolution rate while the remainder of the parameters manipulated in the model do not change significantly across particle size. However, departures in iron release between the model and experiment results indicate that the model does not account for certain variables or processes occurring in the columns. The graphical

representation of R_A versus time showed that a combination of initial surface area and bisulfide concentration cause surface passivation and FeS precipitation.

Examining the role of particle size on iron-sulfur dynamics through a pure end-member experiment conducted in this study could advance knowledge of iron (oxyhydr)oxide nanoparticle reactivity in the environment. Understanding the surface area effects of these particles could play a role in the fate of trace metals and metalloids such as arsenic or lead in groundwater that pose a public health risk (Hochella et al., 2008). Whether these minerals are naturally occurring or engineered for use in permeable reactive barriers, the properties of iron (oxyhydr)oxide nanoparticles are important to consider in the sequestration of contaminants (Plathe et al., 2013).

Nanoparticle physiochemical properties such as sulfidation can be predicted if fundamental studies provide an understanding of particle size controls on surface reactivity. Specifically, the size-dependent kinetics of iron oxide sulfidation could be predictable through a model of type developed in this study. Further, surface passivation due to FeS precipitation is modelled as a function of initial reactive surface area, typically a function of size. These fundamental results have wide-ranging implications.

In Fe-As-S systems in South Asia where elevated arsenic concentrations in groundwater are a major concern, accurate prediction of iron (oxyhydr)oxide reactivity could aid in providing safe drinking water for the population. In engineered remediation solutions such as permeable reactive barriers and *in-situ* precipitation strategies through injection, the model derived here from the advective flow experiments could better determine the efficacy of engineered iron oxide nanoparticles in removing metals and metalloids like arsenic from water. Surface area and particle size are important to consider when developing conclusions about natural systems, which are more complex relative to this study.

REFERENCES

Apte, S. K., Naik, S. D., Sonawane, R. S., Kale, B. B., & Baeg, J. O. (2007). Synthesis of nanosize-necked structure α- and γ-Fe 2O3 and its photocatalytic activity. *Journal of the American Ceramic Society*, *90*(2), 412–414. https://doi.org/10.1111/j.1551-2916.2006.01424.x

Barton, L. E., Grant, K. E., Kosel, T., Quicksall, A. N., & Maurice, P. A. (2011). Size-dependent Pb sorption to nanohematite in the presence and absence of a microbial siderophore. *Environmental Science and Technology*, *45*(8), 3231–3237. https://doi.org/10.1021/es1026135

Benner, S. G., Blowes, D. W., Ptacek, C. J., & Mayer, K. U. (2002). Rates of sulfate reduction and metal sulfide precipitation in a permeable reactive barrier. *Applied Geochemistry*, *17*(3), 301–320. https://doi.org/10.1016/S0883-2927(01)00084-1

Benner, S. G., Hansel, C. M., Wielinga, B. W., Barber, T. M., & Fendorf, S. (2002). Reductive dissolution and biomineralization of iron hydroxide under dynamic flow conditions. *Environmental Science and Technology*, *36*(8), 1705–1711. https://doi.org/10.1021/es0156441

Benner, S. G., Polizzotto, M. L., Kocar, B. D., Ganguly, S., Phan, K., Ouch, K., Sampson, M., & Fendorf, S. (2008). Groundwater flow in an arsenic-contaminated aquifer, Mekong Delta, Cambodia. *Applied Geochemistry*, *23*(11), 3072–3087. https://doi.org/10.1016/j.apgeochem.2008.06.013

Benning, L. G., Wilkin, R. T., & Barnes, H. L. (2000). Reaction pathways in the Fe-S system below 100°C. *Chemical Geology*, *167*(1–2), 25–51. https://doi.org/10.1016/S0009-2541(99)00198-9

Bian, S. W., Mudunkotuwa, I. A., Rupasinghe, T., & Grassian, V. H. (2011). Aggregation and dissolution of 4 nm ZnO nanoparticles in aqueous environments: Influence of pH, ionic strength, size, and adsorption of humic acid. *Langmuir*, *27*(10), 6059–6068. https://doi.org/10.1021/la200570n

Burton, E. D., Johnston, S. G., & Bush, R. T. (2011). Microbial sulfidogenesis in ferrihydrite-rich environments: Effects on iron mineralogy and arsenic mobility. *Geochimica et Cosmochimica Acta*, *75*(11), 3072–3087. https://doi.org/10.1016/j.gca.2011.03.001

Burton, E. D., Johnston, S. G., & Kocar, B. D. (2014). Arsenic mobility during flooding of contaminated soil: The effect of microbial sulfate reduction. *Environmental Science and Technology*, *48*(23), 13660–13667. https://doi.org/10.1021/es503963k

Chernyshova, I. V., Hochella, M. F., & Madden, A. S. (2007). Size-dependent structural transformations of hematite nanoparticles. 1. Phase transition. *Physical Chemistry Chemical Physics*, *9*(14), 1736–1750. https://doi.org/10.1039/b618790k

Chun, C. L., Baer, D. R., Matson, D. W., Amonette, J. E., & Penn, R. L. (2010). Characterization and reactivity of iron nanoparticles prepared with added Cu, Pd, and Ni. *Environmental Science and Technology*, *44*(13), 5079–5085. https://doi.org/10.1021/es903278e

Cline, J. D. (1969). SPECTROPHOTOMETRIC DETERMINATION OF HYDROGEN SULFIDE IN NATURAL WATERS1. *Limnology and Oceanography*, *14*(3), 454–458. https://doi.org/10.4319/lo.1969.14.3.0454

Cooper, D. C., Neal, A. L., Kukkadapu, R. K., Brewe, D., Coby, A., & Picardal, F. W. (2005). Effects of sediment iron mineral composition on microbially mediated changes in divalent metal speciation: Importance of ferrihydrite. *Geochimica et Cosmochimica Acta*, *69*(7), 1739–1754. https://doi.org/10.1016/j.gca.2004.09.013

Cooper, D. C., Picardal, F. F., & Coby, A. J. (2006). Interactions between microbial iron reduction and metal geochemistry: Effect of redox cycling on transition metal speciation in iron bearing sediments. *Environmental Science and Technology*, *40*(6), 1884–1891. https://doi.org/10.1021/es051778t

Darezereshki, E. (2011). One-step synthesis of hematite (α-Fe2O3) nano-particles by direct thermal-decomposition of maghemite. *Materials Letters*, *65*(4), 642–645. https://doi.org/10.1016/j.matlet.2010.11.030

Dickson, D., Liu, G., & Cai, Y. (2017). Adsorption kinetics and isotherms of arsenite and arsenate on hematite nanoparticles and aggregates. *Journal of Environmental Management*, *186*, 261–267. https://doi.org/10.1016/j.jenvman.2016.07.068

El Afifi, E. M., Attallah, M. F., & Borai, E. H. (2016). Utilization of natural hematite as reactive barrier for immobilization of radionuclides from radioactive liquid waste. *Journal of Environmental Radioactivity*, *151*, 156–165. https://doi.org/10.1016/j.jenvrad.2015.10.001

Fan, D., Lan, Y., Tratnyek, P. G., Johnson, R. L., Filip, J., O'Carroll, D. M., Nunez Garcia, A., & Agrawal, A. (2017). Sulfidation of Iron-Based Materials: A Review of Processes and Implications for Water Treatment and Remediation. *Environmental Science and Technology*, *51*(22), 13070–13085. https://doi.org/10.1021/acs.est.7b04177

French, R. A., Jacobson, A. R., Kim, B., Isley, S. L., Penn, L., & Baveye, P. C. (2009). Influence of ionic strength, pH, and cation valence on aggregation kinetics of titanium dioxide nanoparticles. *Environmental Science and Technology*, *43*(5), 1354–1359. https://doi.org/10.1021/es802628n

Gilbert, B., Huang, F., Lin, Z., Goodell, C., Zhang, H., & Banfield, J. F. (2006). Surface chemistry controls crystallinity of ZnS nanoparticles. *Nano Letters*, *6*(4), 605–610. https://doi.org/10.1021/nl052201c

Gilbert, B., Zhang, H., Huang, F., Finnegan, M. P., Waychunas, G. A., & Banfield, J. F. (2003). Special phase transformation and crystal growth pathways observed in nanoparticles. *Geochemical Transactions*, *4*(4), 20–27. https://doi.org/10.1039/b309073f

Goodell, C. M., Gilbert, B., Weigand, S. J., & Banfield, J. F. (2008). Kinetics of water adsorption-driven structural transformation of ZnS nanoparticles. *Journal of Physical Chemistry C*, *112*(13), 4791–4796. https://doi.org/10.1021/jp077189m

Gualtieri, A. F., & Venturelli, P. (1999). In situ study of the goethite-hematite phase transformation by real time synchrotron powder diffraction. *American Mineralogist*, *84*(5–6), 895–904. https://doi.org/10.2138/am-1999-5-624

Hansel, C. M., Benner, S. G., & Fendorf, S. (2005). Competing Fe(II)-Induced Mineralization Pathways of Ferrihydrite. *Environmental Science & Technology*, *39*(18), 7147–7153. https://doi.org/10.1021/es050666z

Hansel, C. M., Benner, S. G., Neiss, J., Dohnalkova, A., Kukkadapu, R. K., & Fendorf, S. (2003). Secondary mineralization pathways induced by dissimilatory iron reduction of ferrihydrite under advective flow. *Geochimica et Cosmochimica Acta*, *67*(16), 2977–2992. https://doi.org/10.1016/S0016-7037(03)00276-X

Hansel, C. M., Benner, S. G., Nico, P., & Fendorf, S. (2004). Structural constraints of ferric (hydr)oxides on dissimilatory iron reduction and the fate of Fe(II). *Geochimica et Cosmochimica Acta*, *68*(15), 3217–3229. https://doi.org/10.1016/j.gca.2003.10.041

Hansel, C. M., Lentini, C. J., Tang, Y., Johnston, D. T., Wankel, S. D., & Jardine, P. M. (2015). Dominance of sulfur-fueled iron oxide reduction in low-sulfate freshwater sediments. *ISME Journal*, *9*(11), 2400–2412. https://doi.org/10.1038/ismej.2015.50

Hellige, K., Pollok, K., Larese-Casanova, P., Behrends, T., & Peiffer, S. (2012). Pathways of ferrous iron mineral formation upon sulfidation of lepidocrocite surfaces. *Geochimica et Cosmochimica Acta*, *81*, 69–81. https://doi.org/10.1016/j.gca.2011.12.014

Hochella, M. F., Lower, S. K., Maurice, P. A., Penn, R. L., Sahai, N., Sparks, D. L., & Twining, B. S. (2008). Nanominerals, Mineral Nanoparticles, and Earth Systems. *Science*, *319*(5870), 1631 LP – 1635. https://doi.org/10.1126/science.1141134

Housaindokht, M. R., & Nakhaei Pour, A. (2012). Study the effect of HLB of surfactant on particle size distribution of hematite nanoparticles prepared via the reverse microemulsion. *Solid State Sciences*, *14*(5), 622–625. https://doi.org/10.1016/j.solidstatesciences.2012.01.016

Isley, S. L., & Penn, R. L. (2008). Titanium dioxide nanoparticles: Effect of sol-gel pH on phase composition, particle size, and particle growth mechanism. *Journal of Physical Chemistry C*, *112*(12), 4469–4474. https://doi.org/10.1021/jp710844d

Keller, A. A., Wang, H., Zhou, D., Lenihan, H. S., Cherr, G., Cardinale, B. J., Miller, R., & Zhaoxia, J. I. (2010). Stability and aggregation of metal oxide nanoparticles in natural aqueous matrices. *Environmental Science and Technology*, *44*(6), 1962–1967. https://doi.org/10.1021/es902987d

Kocar, B. D., Borch, T., & Fendorf, S. (2010). Arsenic repartitioning during biogenic sulfidization and transformation of ferrihydrite. *Geochimica et Cosmochimica Acta*, *74*(3), 980–994. https://doi.org/10.1016/j.gca.2009.10.023

Kumar, N., Lezama Pacheco, J., Noël, V., Dublet, G., & Brown, G. E. (2018). Sulfidation mechanisms of Fe(iii)-(oxyhydr)oxide nanoparticles: A spectroscopic study. *Environmental Science: Nano*, *5*(4), 1012–1026. https://doi.org/10.1039/c7en01109a

Lanzl, C. A., Baltrusaitis, J., & Cwiertny, D. M. (2012). Dissolution of hematite nanoparticle aggregates: Influence of primary particle size, dissolution mechanism, and solution pH. *Langmuir*, *28*(45), 15797–15808. https://doi.org/10.1021/la3022497

Ma, R., Levard, C., Michel, F. M., Brown, G. E., & Lowry, G. V. (2013). Sulfidation mechanism for zinc oxide nanoparticles and the effect of sulfidation on their solubility. *Environmental Science and Technology*, *47*(6), 2527–2534. https://doi.org/10.1021/es3035347

Ma, R., Stegemeier, J., Levard, C., Dale, J. G., Noack, C. W., Yang, T., Brown, G. E., & Lowry, G. V. (2014). Sulfidation of copper oxide nanoparticles and properties of resulting copper sulfide. *Environmental Science: Nano*, *1*(4), 347–357. https://doi.org/10.1039/c4en00018h

Madden, A. S., Hochella, M. F., & Luxton, T. P. (2006). Insights for size-dependent reactivity of hematite nanomineral surfaces through Cu2+ sorption. *Geochimica et Cosmochimica Acta*, *70*(16), 4095–4104. https://doi.org/10.1016/j.gca.2006.06.1366

Majzlan, J., Grevel, K. D., & Navrotsky, A. (2003). Thermodynamics of Fe oxides: Part II. Enthalpies of formation and relative stability of goethite (α-FeOOH), lepidocrocite (γ-FeOOH), and maghemite (γ-Fe2O3). *American Mineralogist*, *88*(5), 855–859. https://doi.org/10.2138/am-2003-5-614

Mazeina, L., & Navrotsky, A. (2007). Enthalpy of water adsorption and surface enthalpy of goethite (α-FeOOH) and hematite (α-Fe2O3). *Chemistry of Materials*, *19*(4), 825–833. https://doi.org/10.1021/cm0623817

Michel, F. M., Ehm, L., Antao, S. M., Lee, P. L., Chupas, P. J., Liu, G., Strongin, D. R., Schoonen, M. A. A., Phillips, B. L., & Parise, J. B. (2007). The Structure of Ferrihydrite, a Nanocrystalline Material. *Science*, *316*(5832), 1726–1729. https://doi.org/10.1126/science.1142525

Michel, F. M., Ehm, L., Liu, G., Han, W. Q., Antao, S. M., Chupas, P. J., Lee, P. L., Knorr, K., Eulert, H., Kim, J., Grey, C. P., Celestian, A. J., Gillow, J., Schoonen, M. A. A., Strongin, D. R., & Parise, J. B. (2007). Similarities in 2- and 6-Line Ferrihydrite Based on Pair Distribution Function Analysis of X-ray Total Scattering. *Chemistry of Materials*, *19*(6), 1489–1496. https://doi.org/10.1021/cm062585n

Morse, J. W., & Arakaki, T. (1993). Adsorption and coprecipitation of divalent metals with mackinawite (FeS). *Geochimica et Cosmochimica Acta*, *57*(15), 3635–3640. https://doi.org/10.1016/0016-7037(93)90145-M

Nakhaei Pour, A., Housaindokht, M. R., Irani, M., & Kamali Shahri, S. M. (2014). Size-dependent studies of Fischer-Tropsch synthesis on iron based catalyst: New kinetic model. *Fuel*, *116*, 787–793. https://doi.org/10.1016/j.fuel.2013.08.080

Nasrazadani, S. (1997). The application of infrared spectroscopy to a study of phosphoric and tannic acids interactions with magnetite (Fe3O4), goethite (α-FeOOH) and lepidocrocite (γ-FeOOH). *Corrosion Science*, *39*(10–11), 1845–1859. https://doi.org/10.1016/S0010-938X(97)00060-7

Navrotsky, A., Mazeina, L., & Majzlan, J. (2008). Size-Driven Structural and Thermodynamic Complexity in Iron Oxides. *Science*, *319*(5870), 1635–1638. https://doi.org/10.1126/science.1148614

Neal, A. L., Techkarnjanaruk, S., Dohnalkova, A., McCready, D., Peyton, B. M., & Geesey, G. G. (2001). Iron sulfides and sulfur species produced at hematite surfaces in the presence of sulfate-reducing bacteria. *Geochimica et Cosmochimica Acta*, *65*(2), 223–235. https://doi.org/10.1016/S0016-7037(00)00537-8

Nordstrom, D. K., Alpers, C. N., Ptacek, C. J., & Blowes, D. W. (2000). Negative pH and extremely acidic mine waters from Iron Mountain, California. *Environmental Science and Technology*, *34*(2), 254–258. https://doi.org/10.1021/es990646v

O'Day, P. A., Vlassopoulos, D., Root, R., & Rivera, N. (2004). The influence of sulfur and iron on dissolved arsenic concentrations in the shallow subsurface under changing redox conditions. *Proceedings of the National Academy of Sciences of the United States of America*, *101*(38), 13703–13708. https://doi.org/10.1073/pnas.0402775101

Papacostas, N. C., Bostick, B. C., Quicksall, A. N., Landis, J. D., & Sampson, M. (2008). Geomorphic controls on groundwater arsenic distribution in the Mekong River Delta, Cambodia. *Geology*, *36*(11), 891–894. https://doi.org/10.1130/G24791A.1

Penn, R. L. (2004). Kinetics of oriented aggregation. *Journal of Physical Chemistry B*, *108*(34), 12707–12712. https://doi.org/10.1021/jp036490

Penn, R. L., & Banfield, J. F. (1998). Imperfect Oriented Attachment: Dislocation Generation in Defect-Free Nanocrystals. *Science*, *281*(5379), 969–971. https://doi.org/10.1126/science.281.5379.969

Plathe, K. L., von der Kammer, F., Hassellöv, M., Moore, J. N., Murayama, M., Hofmann, T., & Hochella, M. F. (2013). The role of nanominerals and mineral nanoparticles in the transport of toxic trace metals: Field-flow fractionation and analytical TEM analyses after nanoparticle isolation and density separation. *Geochimica et Cosmochimica Acta*, *102*, 213–225. https://doi.org/10.1016/j.gca.2012.10.029

Polizzotto, M. L., Kocar, B. D., Benner, S. G., Sampson, M., & Fendorf, S. (2008). Near-surface wetland sediments as a source of arsenic release to ground water in Asia. *Nature*, *454*(7203), 505–508. https://doi.org/10.1038/nature07093

Poulton, S. W., Krom, M. D., & Raiswell, R. (2004). A revised scheme for the reactivity of iron (oxyhydr)oxide minerals towards dissolved sulfide. *Geochimica et Cosmochimica Acta*, *68*(18), 3703–3715. https://doi.org/10.1016/j.gca.2004.03.012

Quicksall, A. N., Bostick, B. C., & Sampson, M. L. (2008). Linking organic matter deposition and iron mineral transformations to groundwater arsenic levels in the Mekong delta, Cambodia. *Applied Geochemistry*, *23*(11), 3088–3098. https://doi.org/10.1016/j.apgeochem.2008.06.027

Raiswell, R. (2011). Iron transport from the continents to the open ocean: The aging-rejuvenation cycle. *Elements*, *7*(2), 101–106. https://doi.org/10.2113/gselements.7.2.101

Rickard, D. (1995). Kinetics of FeS precipitation: Part 1. Competing reaction mechanisms. *Geochimica et Cosmochimica Acta*, *59*(21), 4367–4379. https://doi.org/10.1016/0016-7037(95)00251-T

Rickard, D. (1997). Kinetics of pyrite formation by the H2S oxidation of iron (II) monosulfide in aqueous solutions between 25 and 125°C: The rate equation. *Geochimica et Cosmochimica Acta*, *61*(1), 115–134. https://doi.org/10.1016/s0016-7037(96)00321-3

Robie, R., & Hemingway, B. (1995). *Thermodynamic properties of minerals and related substances at 298.15 K and 1 bar (10^5 pascals) pressure and at higher temperatures*. https://doi.org/10.3133/b2131

Rout, K., Mohapatra, M., & Anand, S. (2012). 2-Line ferrihydrite: Synthesis, characterization and its adsorption behaviour for removal of Pb(ii), Cd(ii), Cu(ii) and Zn(ii) from aqueous solutions. *Dalton Transactions*, *41*(11), 3302–3312. https://doi.org/10.1039/c2dt11651k

Ruan, H. D., Frost, R. L., & Kloprogge, J. T. (2001). The behavior of hydroxyl units of synthetic goethite and its dehydroxylated product hematite. *Spectrochimica Acta - Part A: Molecular and Biomolecular Spectroscopy*, *57*(13), 2575–2586. https://doi.org/10.1016/S1386-1425(01)00445-0

Saalfield, S. L., & Bostick, B. C. (2009). Changes in iron, sulfur, and arsenic speciation associated with bacterial sulfate reduction in ferrihydrite-rich systems. *Environmental Science and Technology*, *43*(23), 8787–8793. https://doi.org/10.1021/es901651k

Schwertmann, U., & Cornell, R. M. (2001). *Iron Oxides in the Laboratory (Second Edition)*.

Schwertmann, U., & Murad, E. (1983). Effect of pH on the formation of goethite and hematite from ferrihydrite. *Clays & Clay Minerals*, *31*(4), 277–284. https://doi.org/10.1346/CCMN.1983.0310405

Seehra, M. S., Roy, P., Raman, A., & Manivannan, A. (2004). Structural investigations of synthetic ferrihydrite nanoparticles doped with Si. *Solid State Communications*, *130*(9), 597–601. https://doi.org/10.1016/j.ssc.2004.03.022

Skinner, H. C. W. (2005). Biominerals. *Mineralogical Magazine*, *69*(5), 621–641. https://doi.org/10.1180/0026461056950275

Smedley, P. L., & Kinniburgh, D. G. (2002). A review of the source, behaviour and distribution of arsenic in natural waters. *Applied Geochemistry*, *17*(5), 517–568. https://doi.org/10.1016/S0883-2927(02)00018-5

Tadic, M., Trpkov, D., Kopanja, L., Vojnovic, S., & Panjan, M. (2019). Hydrothermal synthesis of hematite (α-Fe2O3) nanoparticle forms: Synthesis conditions, structure, particle shape analysis, cytotoxicity and magnetic properties. *Journal of Alloys and Compounds*, *792*, 599–609. https://doi.org/10.1016/j.jallcom.2019.03.414

Townsend, L. T., Shaw, S., Ofili, N. E. R., Kaltsoyannis, N., Walton, A. S., Mosselmans, J. F. W., Neill, T. S., Lloyd, J. R., Heath, S., Hibberd, R., & Morris, K. (2019). Formation of a U(VI)-Persulfide Complex during Environmentally Relevant Sulfidation of Iron (Oxyhydr)oxides. *Environmental Science and Technology*. https://doi.org/10.1021/acs.est.9b03180

Walter, D., Buxbaum, G., & Laqua, W. (2001). The mechanism of the thermal transformation from goethite to hematite*. *Journal of Thermal Analysis and Calorimetry*, *63*(3), 733–748. https://doi.org/10.1023/A:1010187921227

Wolthers, M., Butler, I. B., & Rickard, D. (2007). Influence of arsenic on iron sulfide transformations. *Chemical Geology*, *236*(3–4), 217–227. https://doi.org/10.1016/j.chemgeo.2006.09.010

Wolthers, M., Charlet, L., van Der Linde, P. R., Rickard, D., & van Der Weijden, C. H. (2005). Surface chemistry of disordered mackinawite (FeS). *Geochimica et Cosmochimica Acta*, *69*(14), 3469–3481. https://doi.org/10.1016/j.gca.2005.01.027

Xiao, W., Jones, A. M., Collins, R. N., Bligh, M. W., & Waite, T. D. (2017). Use of fourier transform infrared spectroscopy to examine the Fe(II)-Catalyzed transformation of ferrihydrite. *Talanta*, *175*(July), 30–37. https://doi.org/10.1016/j.talanta.2017.07.018

Xu, C., Deng, K., Li, J., & Xu, R. (2015). Impact of environmental conditions on aggregation kinetics of hematite and goethite nanoparticles. *Journal of Nanoparticle Research*, *17*(10), 1–13. https://doi.org/10.1007/s11051-015-3198-8

Yao, W., & Millero, F. J. (1996). Oxidation of hydrogen sulfide by hydrous Fe(III) oxides in seawater. *Marine Chemistry*, *52*(1), 1–16. https://doi.org/10.1016/0304-4203(95)00072-0

Yee, N., Shaw, S., Benning, L. G., & Nguyen, T. H. (2006). The rate of ferrihydrite transformation to goethite via the Fe(II) pathway. *American Mineralogist*, *91*(1), 92–96. https://doi.org/10.2138/am.2006.1860

Zamiri, R., Ahangar, H. A., Zakaria, A., Zamiri, G., Bahari, H. R., & Drummen, G. P. C. (2014). Hydrothermal synthesis of goethite (α-FeOOH) nanorods in the presence of ethylenediamine:thiourea. *Journal of Nanoparticle Research*, *16*(4). https://doi.org/10.1007/s11051-014-2333-2

Zhang, H., Gilbert, B., Huang, F., & Banfield, J. F. (2003). Water-driven structure transformation in nanoparticles at room temperature. *Nature*, *424*(6952), 1025–1029. https://doi.org/10.1038/nature01845

APPENDIX

Appendix A. Nanoparticle Suspension Characterization

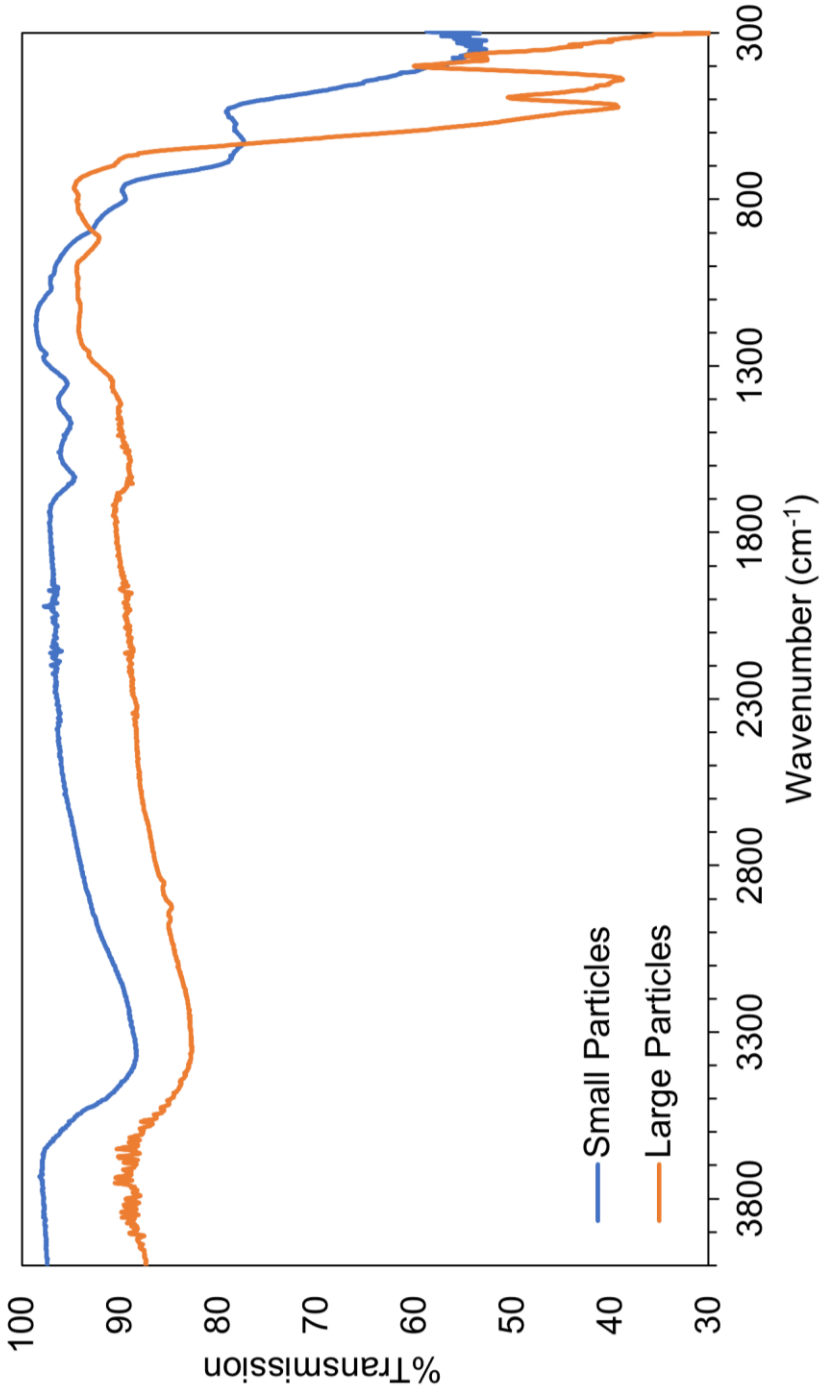

Figure A1. Full IR spectra for large and small particles from 250 to 4000 cm-1

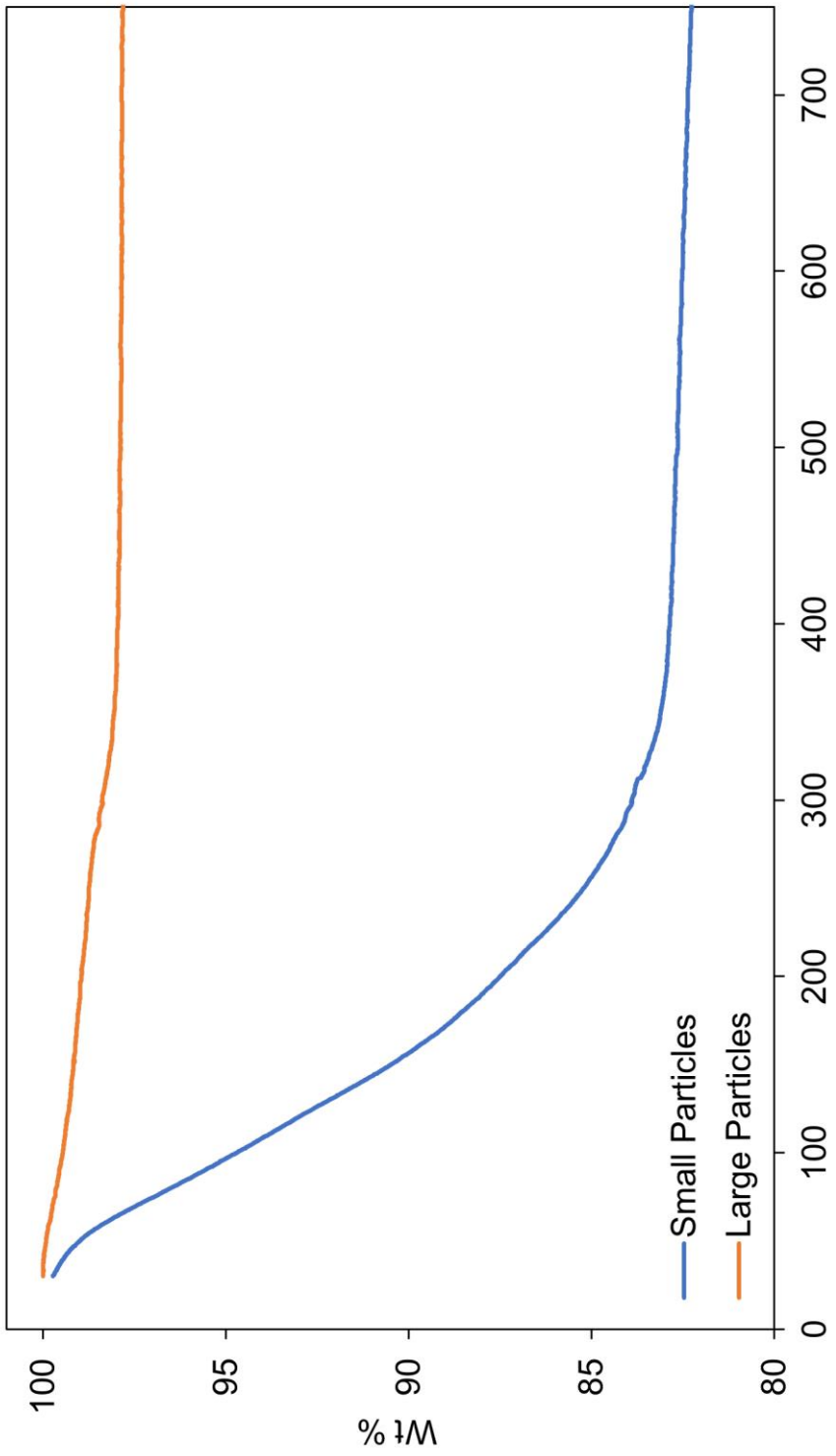

Figure A2. Full TGA thermogram for large and small particles from 30 to 800°C.

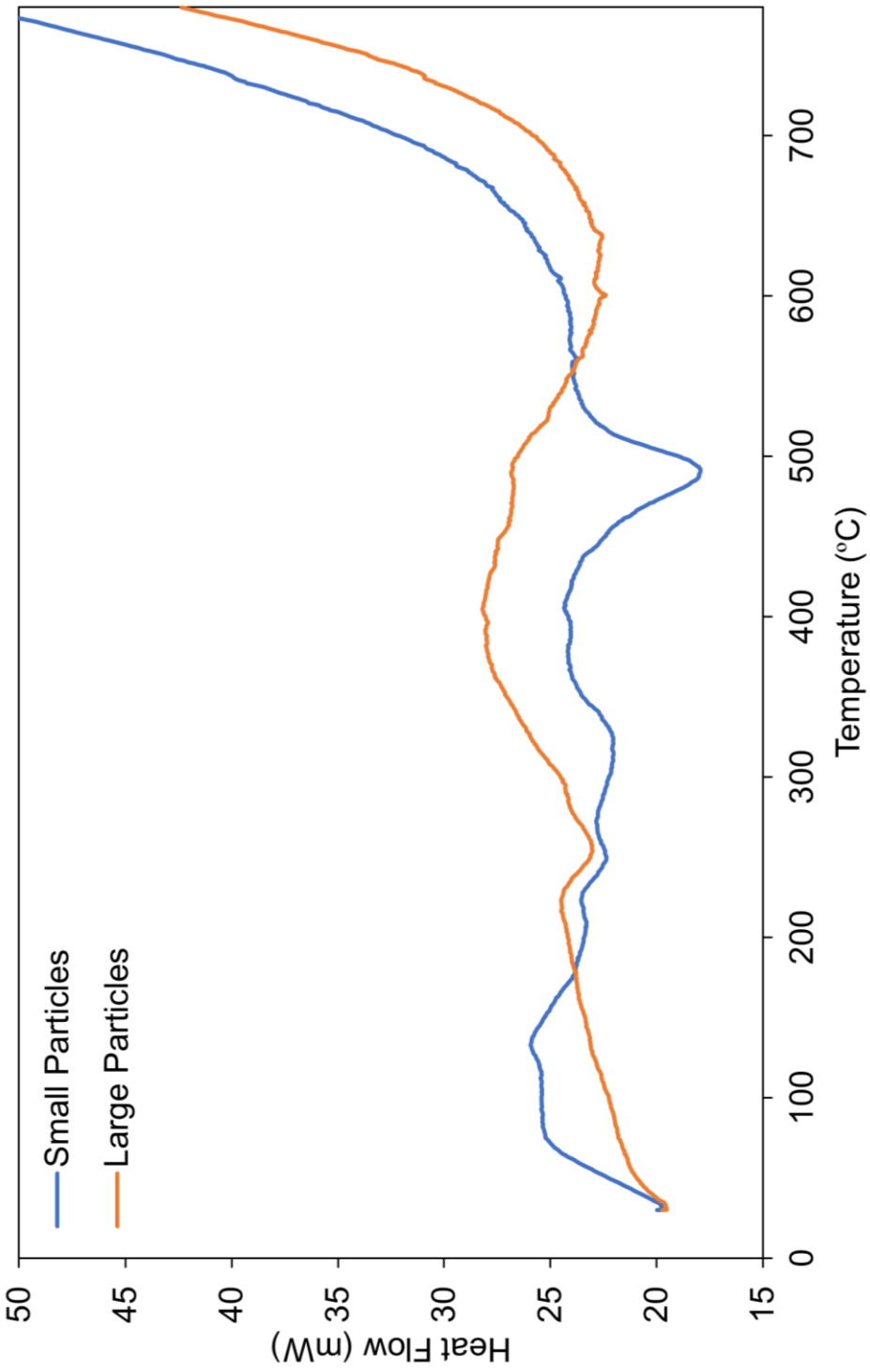

Figure A3. Full DSC thermogram for large and small particles from 30 to 800°C.

Appendix B. Batch Experiments

Batch experiments show a relationship between bisulfide concentration and particle size through elemental analysis and physical changes to the hematite nanoparticles during reaction. Figures 7A and 7B demonstrate that suspension color in the tubes of coated sands for small and large particles darken as bisulfide concentration increases. Only reaction between the small particle-coated sand and 32 mM bisulfide produced a black precipitate indicative of iron sulfide formation. This physical change was not observed for large particles reacted with 32 mM bisulfide and suggests that sulfidation of hematite nanoparticles and precipitation of iron sulfide is size-dependent. Table 4 shows that the increase in reduced iron concentrations with increasing bisulfide concentration is consistent with physical observations except for the reaction between large particles and 32 mM bisulfide. Bisulfide concentrations of 0.31 mM and above produced higher iron concentrations for smaller particles. Further experimentation is necessary to determine if iron release is greater for large particles than small particles at lower bisulfide concentrations and if iron concentrations are consistently lower for large particles reacted with 32 mM bisulfide. ICP-MS results for this experiment were quantifiable except for the reaction between small particles and 32 mM bisulfide, where raw counts were beyond the calibrant range. Overall, the physical changes and reduced iron concentration in each experiment indicate that hematite reactivity is greater for small particles with increasing bisulfide concentration.

Figure B1. Physical changes resulting from reaction between bisulfide ranging in concentration from 0.0032 mM to 32 mM and nanoparticle hematite-coated sands for small (A) and large (B) particles.

Table B1. Ferrous iron concentrations from sulfidation of hematite nanoparticles at varying bisulfide concentrations in batch reaction.

Bisulfide concentration (mM)	Ferrous iron concentration (mM)	
	Small Particles	Large Particles
0.0032	0.00020	0.00052
0.032	0.00070	0.0012
0.32	0.043	0.0038
3.2	0.072	0.020
32	0.18	0.013

Appendix C. Rubidium in Effluent from Column Experiments

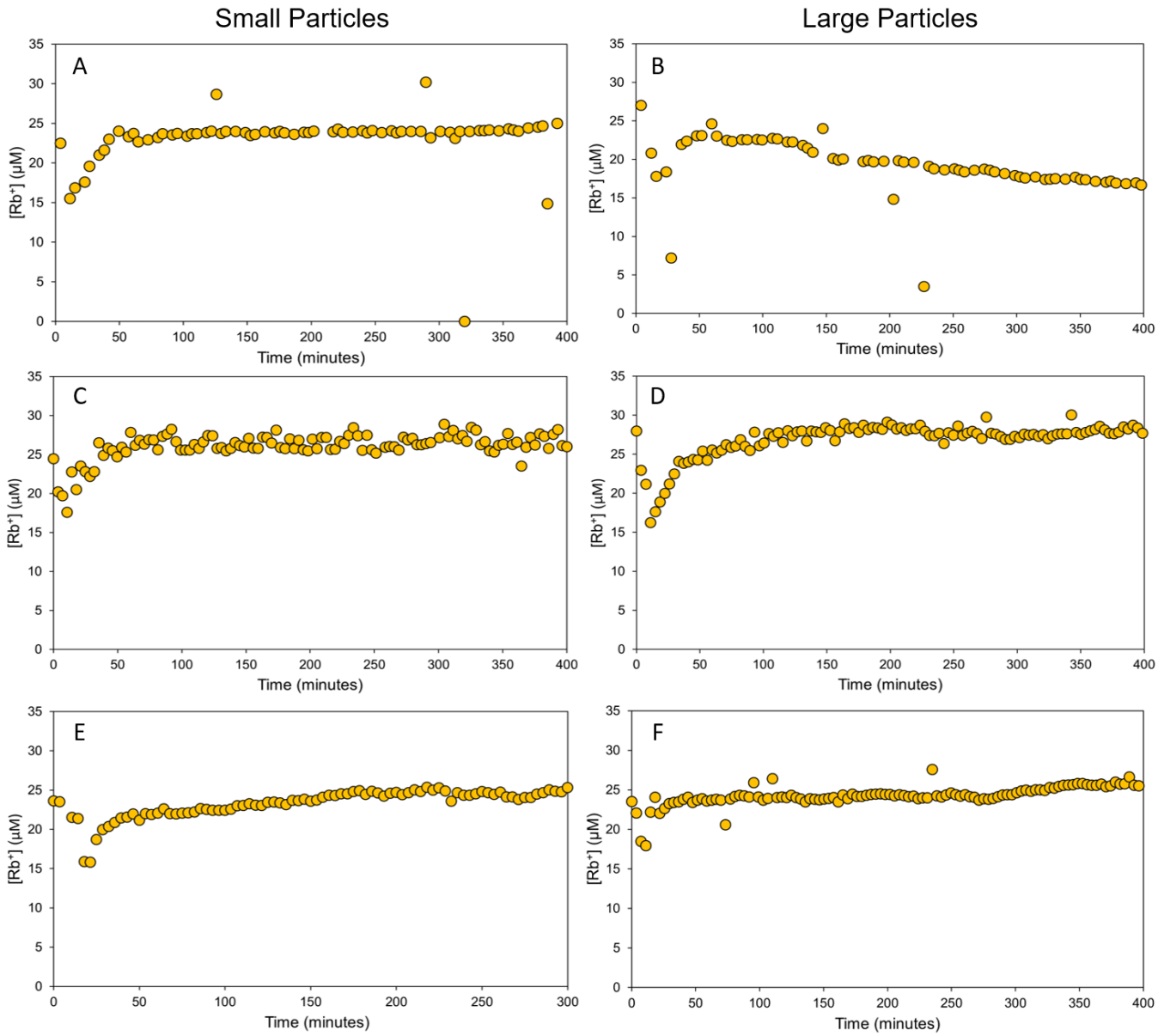

Figure C1. Rb^+ elution across 0.1 mM (A and B), 1 mM (C and D), and 10 mM (E and F). Concentrations briefly decline in the first 20 minutes of reaction with bisulfide solution but achieve near constant values that are significantly higher than the ferrous iron concentrations in the effluent.

Appendix D. Integrated Kinetic Rate Model Column Experiment Results

Table D1. Values for parameters across all column experiments

Parameters	Small Particles			Large Particles		
Bisulfide concentration	10 mM	1 mM	0.1 mM	10 mM	1 mM	0.1 mM
log k_{Fe}	-7.3	-8.0	-8.3	-6.0	-6.4	-6.3
log k_{FeS}	1.5	1.7	1.2	1.2	1.5	1.5
log k_A	-2.3	-3.0	-2.8	-2.1	-3.0	-2.5
log $[HS^-]_0$	4.0	3.0	2.0	4.0	3.0	2.0
n_1	0.6	0.6	0.5	0.6	0.6	0.6
n_2	1.4	1.0	1.0	1.1	1.0	1.0
log($-C_1$)	-4.4	-5.6	-4.9	-5.0	-5.3	-5.1
log($-C_1$*)	-4.4	-5.5	-4.9	-4.9	-5.3	-5.1